Marine Geology 465 (2023) 107146

Contents lists available at ScienceDirect

Marine Geology

journal homepage: www.elsevier.com/locate/margo

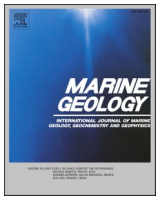

Research Article

Coastal response to Holocene Sea-level change: A case study from Singapore

Stephen Chua [a,*], Adam D. Switzer [a,b], Chris Gouramanis [c], Yama Dixit [d], Michael I. Bird [e,f], Benjamin P. Horton [a,b]

[a] Earth Observatory of Singapore, Nanyang Technological University, Singapore, 50 Nanyang Ave, S639798, Singapore
[b] Asian School of the Environment, Nanyang Technological University, Singapore, 62 Nanyang Dr, S637459, Singapore
[c] Research School of Earth Sciences, Australian National University, Canberra, ACT 0200, Australia
[d] Centre for Atmospheric Sciences, Indian Institute of Technology, Delhi, India
[e] College of Science and Engineering and ARC Centre of Excellence for Australian Biodiversity and Heritage, James Cook University, Cairns, QLD 4870, Australia
[f] College of Science and Engineering, James Cook University, Cairns, QLD 4870, Australia

ARTICLE INFO

Editor: Prof Edward Anthony

Keywords:
Coastal evolution
Sediments
Delta
Estuary
Geochemistry
Age-depth modelling
Accommodation space
Coastal protection

ABSTRACT

The deceleration of early to mid-Holocene (10–7 cal. ka BP) relative sea-level rise (RSLR) played a key role in transforming coastal systems from estuaries to deltas. Palaeoenvironmental reconstruction of coastal evolution provide case studies that can help project the response of modern coastal systems to future RSLR. The response of deltas to future RSLR is particularly important to South, Southeast and East Asia which collectively contain 71% of the global coastal population living below 10 m in elevation and 75% of the global coastal floodplain population. However, few Holocene studies of equatorial delta systems exist.

Here, we investigate the early to mid-Holocene coastal response to decelerating rates of RSLR through palaeoenvironmental reconstruction of the Kallang River Basin, Singapore. We produce a multi-proxy (sedimentology, stable carbon isotope, XRF elemental ratios) record from sediment core MSBH01B to compare with the Holocene relative sea-level record for Singapore. We identify different phases of coastal response through the interplay between accommodation space (A) driven predominantly by RSLR and sedimentation rate (S).

In the early Holocene rapid RSLR coupled with low sedimentation rates ($A/S = 5.1 \pm 0.3$) led to mangrove disappearance in the Kallang River Basin coastal area within ~300 years (9.5–9.2 cal. ka BP). Estuarine sediments were deposited from 9.2 to 8.8 cal. ka BP during continued high rates of RSLR coupled with highest sedimentation rates ($A/S = 3.1 \pm 0.8$) as the coastline retreated. Prodelta sediments were deposited from 8.8 to 8.2 cal. ka BP during decreasing rate of RSLR and high sedimentation rates ($A/S = 4.6 \pm 5.2$). Delta front sediments were deposited during this delta initiation phase from 8.2 to 7.6 cal. ka BP as during a period of low and consistent RSLR and sedimentation rates ($A/S = 1.7 \pm 0.2$). Finally, a prograding delta started forming from 7.6 to 7.2 cal. ka BP during lowest rates of RSLR and sedimentation rates ($A/S = 1.7 \pm 0.2$). Our record provides a case study of possible responses of modern delta systems under a spectrum of predicted sea-level rise scenarios and accompanying sedimentation rates. This study provides an estimated threshold A/S value of 1.7 for coastal retreat to inform policy and mitigation/adaptation measures for Singapore and a simple methodology to obtain local threshold values of other equatorial cities built on floodplain and/or delta systems.

1. Introduction

Early to mid-Holocene (10–7 cal. ka BP) relative sea-level rise (RSLR) has played a main role in transforming coastal systems from estuaries to deltas (e.g., Stanley and Warne, 1994; Hori and Saito, 2007; Zong et al., 2012). The slowing in the rate of RSLR permitted coastal processes to rework sediment and control sediment accumulation in various coastal morphologies (e.g., Tamura et al., 2009; Ishii et al., 2021). Rates of RSLR of up to ~15 mm/yr during the early to mid-Holocene (Lambeck et al., 2014) are due to rapid melting of the Laurentide and Fennoscandian ice sheets (Stroeven et al., 2016; Ullman et al., 2016). These values fall within the range of predictions for the latter part of the 21st century

* Corresponding author at: Earth Observatory of Singapore, Nanyang Technological University, Block N2-01a-09, 50 Nanyang Drive, S(639798), Singapore.
E-mail address: stephen.chua@ntu.edu.sg (S. Chua).

https://doi.org/10.1016/j.margeo.2023.107146
Received 6 June 2023; Received in revised form 7 September 2023; Accepted 10 September 2023
Available online 12 September 2023

(Fox-Kemper et al., 2021). Therefore, early to mid-Holocene palaeoenvironmental studies on the largest deltas, such as the Mississippi (e.g., Törnqvist et al., 2004; Blum and Roberts, 2009; Törnqvist et al., 2020), the Yangtze (e.g., Song et al., 2013; Gao et al., 2019; Wang et al., 2018) and the Nile (e.g., Bernhardt et al., 2012; Pennington et al., 2017), provide evidence of the potential response of these coastal systems to future sea-level rise.

The response of deltas to future sea-level rise is particularly important to South, Southeast and East Asia which collectively contain 71% of the global coastal population living below 10 m in elevation (546 million out of 768 million people globally) and 75% of the global coastal floodplain population (185 million out of 249 million people globally) (Nicholls et al., 2021). The majority of these people live in megacities built on large deltas (Syvitski et al., 2009). Several studies have examined the early to mid-Holocene evolution of Southeast Asian deltas, including the Mekong delta in southern Vietnam (e.g., Lap Nguyen et al., 2000; Ta et al., 2002; Tamura et al., 2009; Tjallingii et al., 2010; Hanebuth et al., 2012; Ishii et al., 2021), the Song Hong (Red River) delta in northern Vietnam (e.g., Tanabe, 2003; Tanabe et al., 2006; Andreas et al., 2017; Duong et al., 2020) and the Chao Phraya delta in Thailand (e.g., Sinsakul, 2000; Tanabe et al., 2003). The Holocene evolution of Asian deltas have been primarily reconstructed based on detailed sedimentological analysis and radiocarbon dating of sediment cores (e.g., Tanabe et al., 2003; Hori and Saito, 2007; Hanebuth et al., 2012; Giosan et al., 2018) and seismic surveys (e.g., Schimanski and Stattegger, 2005; Xue et al., 2010; Yen et al., 2021). However, there are few studies of equatorial delta systems compared to other temperate or subtropical regions (e.g., Marcott et al., 2013; Bova et al., 2021).

Here, we investigate the coastal evolution of the Kallang River Basin in southern Singapore during the early to mid-Holocene. We reconstruct the paleoenvironment from a multi-proxy (sedimentology, microfossil, XRF-scanning elemental ratios, stable carbon isotope measurements) examination of a sediment core that records the geomorphological evolution of the southern coast of Singapore. We compare the paleoenvironmental reconstructions with a Holocene relative sea-level record for Singapore that contains >40 sea-level index points between 9.5 and 7.2 cal. ka BP (Chua et al., 2021), where rates of RSL rise are constrained with the Error-In-Variables Integrated Gaussian Process (EIV-IGP) model (Cahill et al., 2015). We identify different coastal response phases using the *A/S* method (Muto and Steel, 1997) to understand the

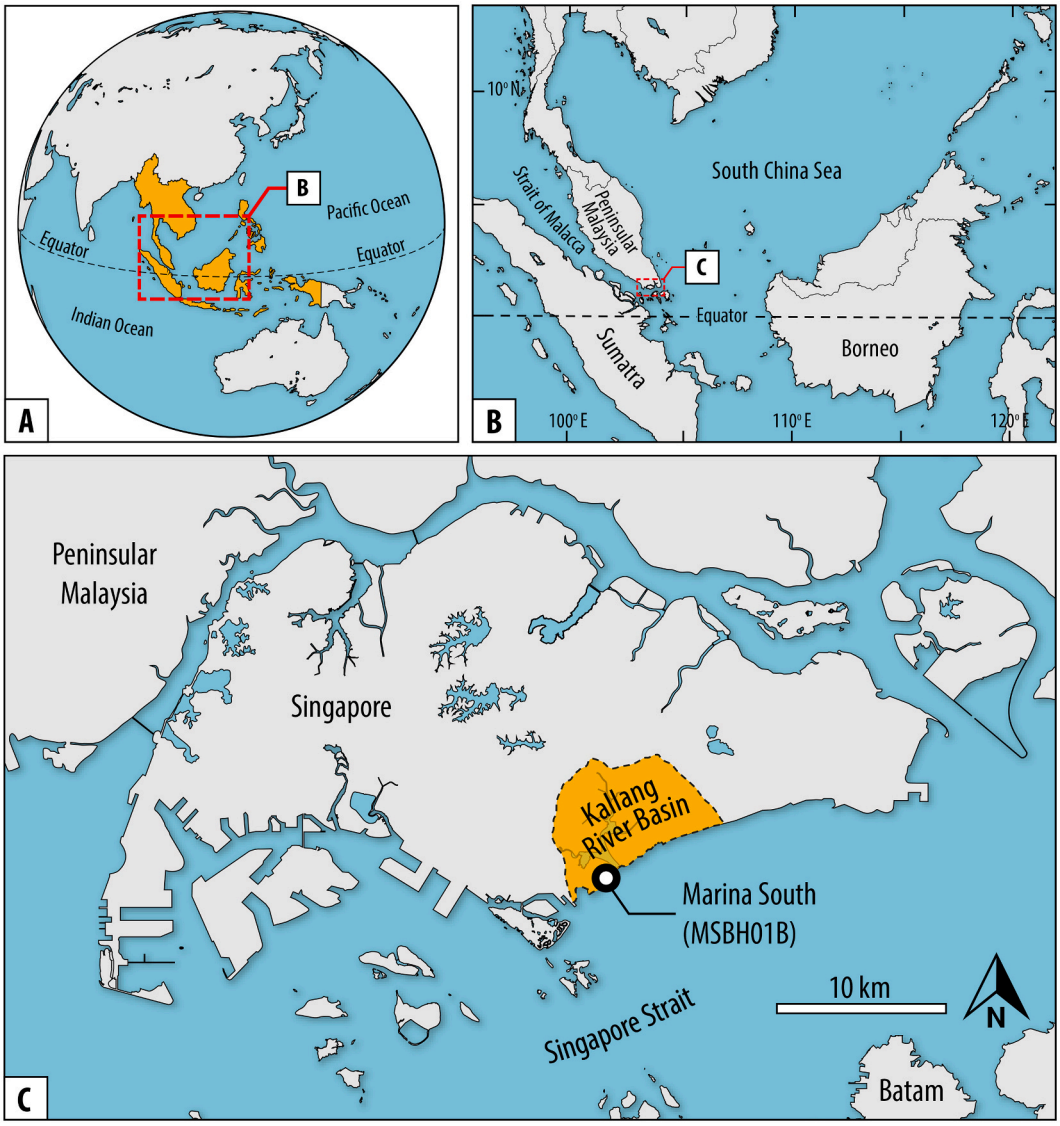

Fig. 1. (A) Globe with Southeast Asia shaded in yellow. (B) Regional map of Southeast Asia with red box showing location of Singapore (C) Map of Singapore showing the location of sediment core MSBH01B at Marina South. The irregular yellow polygon represents the extent of the Kallang River Basin. (For interpretation of the references to colour in this figure legend, the reader is referred to the web version of this article.)

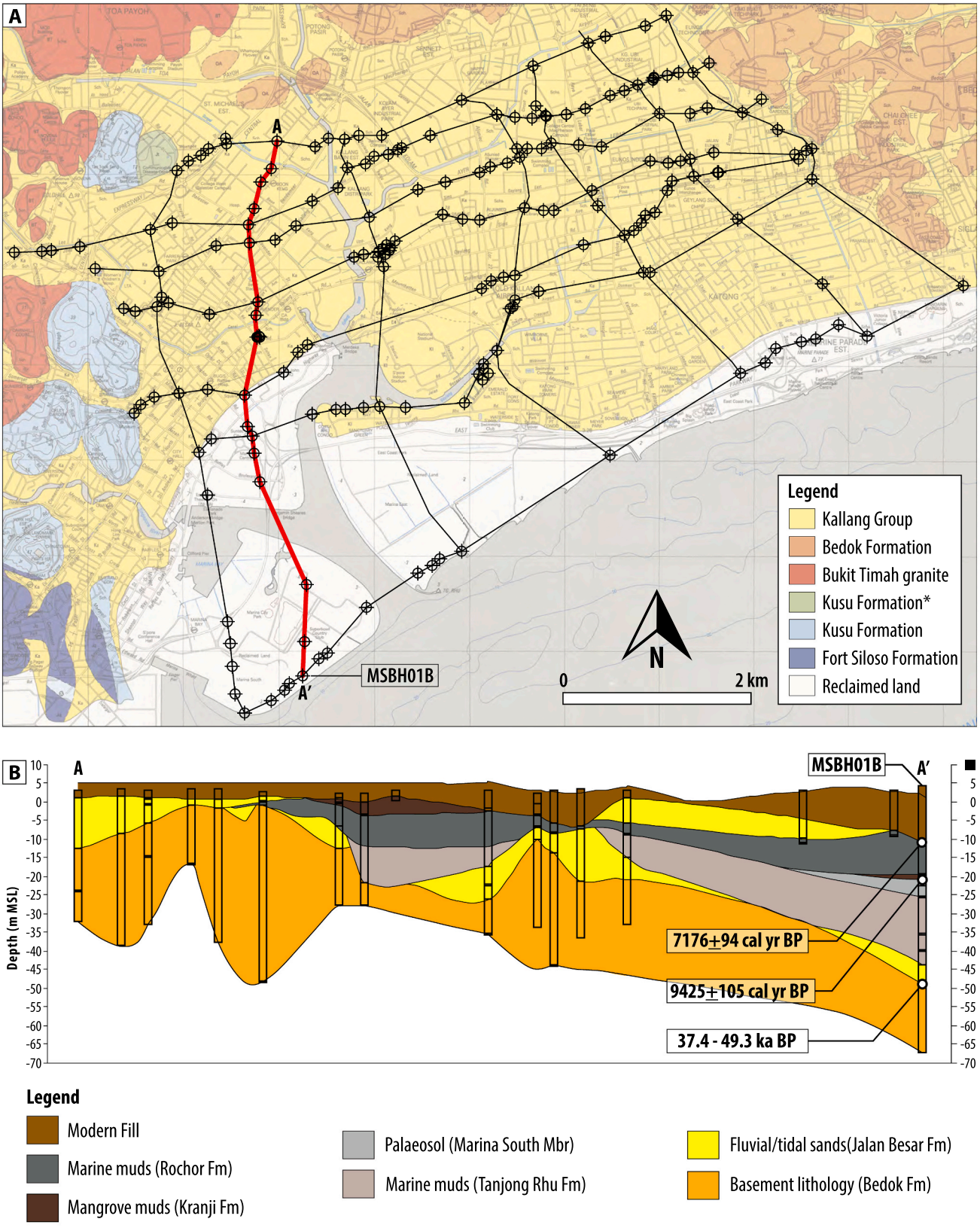

Fig. 2. (A) Selection of boreholes for creating cross sections for the Kallang River Basin (modified from Chua et al., 2020). Red line denotes Transect A–A' with sediment core MSBH01B as seaward limit. White coastal areas represent the extent of reclaimed land. *Green region has been reclassified as Kusu Formation in Leslie et al. (2021). (B) Cross-section of Transect A- A' showing the local stratigraphic succession and location of MSBH01B. The vertical exaggeration of the cross-section is set at 25 times (modified from Chua et al., 2020). (For interpretation of the references to colour in this figure legend, the reader is referred to the web version of this article.)

interplay between accommodation space (*A*), driven predominantly by SLR (Törnqvist et al., 2021), and sedimentation rate (*S*). Our record of coastal response in the early to mid-Holocene to RSL change provides a case study recording the possible responses of modern delta systems under a spectrum of predicted sea-level rise scenarios and accompanying sedimentation rates (Fox-Kemper et al., 2021).

2. Study area

Singapore is a small island state located at the tip of Peninsular Malaysia between latitude 1°09′N and 1°29′N and longitude 103°36′E and 104°06′E. The geology of Singapore comprises basement igneous intrusions emplaced during the Permian (~285 Ma) to Triassic Period (~240 Ma), overlain by sedimentary rock of fluvial/shallow marine origin during the Triassic to Cretaceous Period (~120 Ma) and younger unlithified sediments during the Quaternary Period (2.6 Ma) (Dodd et al., 2019). The geology of Singapore forms part of Sundaland that comprises continental blocks and volcanic arcs that formed the igneous intrusions, and separated by suture zones that represent closed ocean basins (Gillespie et al., 2019).

Singapore sits in the core of Sundaland (Simons et al., 2007) (Fig. 1B), which is generally considered tectonically stable, being distal from major plate convergence/subduction zones (Tjia and Liew, 1996). Some studies suggest a subsidence rate of 0.06 to 0.19 mm/year since the beginning of the Last Glacial Maximum (LGM) (Bird et al., 2006), and from 0.2 to 0.3 mm/year through the Pleistocene (Sarr et al., 2019), hypothesised to be due to underlying mantle flow leading to dynamic but transient topographic changes. Occurrence of such vertical deformation is also concentrated at more exterior collision or subduction zones, with modern GPS (Global Positioning System) recording negligible internal deformation (e.g., Simons et al., 2007). Sundaland was largely exposed when RSL was ~120 m below present during the Last Glacial Maximum approximately 20,000 years ago (Shaw et al., 2023; Hanebuth et al., 2009). Subsequent SLR led to the inundation and subsequent infilling of relict palaeochannels and coastal plains on the outer and middle Sunda Shelf, including the Straits of Singapore, processes that defined the modern Southeast Asian coastline (Bird et al., 2006).

The Kallang River Basin is located in the southern region of Singapore (Fig. 1C, 2A). Singapore's Central Business District as well as other key infrastructure are located in this topographically low-lying area (Chua et al., 2020). The north-south coast-perpendicular profile (Fig. 2B) shows two thick successions of marine muds with a basal unit of littoral sands (Chua et al., 2020). The lower marine mud unit (Tanjung Rhu Member) was deposited during a period of high sea levels approximately during the late Pleistocene (~125,000 years ago) (Chua et al., 2020; Leslie et al., 2021). The top of the Tanjung Rhu Member marine muds was exposed and desiccated during the Last Interglacial forming the palaeosol of the Marina South Member (Chua et al., 2020; Leslie et al., 2021). Organic-rich units (Kranji Formation), marine muds (Rochor Member) and fluvial/littoral sands (Jalan Besar Formation) were subsequently deposited from 9.5 cal. ka BP to present (Chua et al., 2020; Leslie et al., 2021).

Our core site at Marina South, near the entrance of the Kallang River Basin (Fig. 2A), is a coastal area that was reclaimed as recently as 1985 (Chew and Wei, 1980). Based on an 1846 topographical map, Marina South was a lagoonal river mouth fronted by elongate sandbars and flats and fed by three converging tributaries of the Kallang River Basin that drained from the granitic hills in central Singapore (Chua et al., 2020). This granite is an acidic igneous rock composed predominantly of quartz (30%) and feldspar (60%) (Sharma et al., 1999). High amounts of iron are leached differentially from inland highly-weathered, iron-rich plutons of the Bukit Timah Granite (Leslie et al., 2019). These central granite highlands are the headwater source of iron-rich terrigenous sediments for the Kallang River Basin in southern Singapore.

Coastal waters of Singapore are shallow (< 30 m deep), except for a localised depression of up to 200 m along the Straits of Singapore (Bird et al., 2006). The mean tidal range of Singapore is 2.4 m and 1 m during spring and neap tides, respectively (Wong, 1992). Singapore has a short wave fetch, which produces low energy wave conditions with breaker heights of <20 cm (Chia et al., 1988). The coastline of pre-development Singapore was characterised by dense intertidal mangrove forests (Corlett, 1992). Intensive urbanisation has greatly altered the coastline and nearshore regions resulting in nearly 25% reclaimed land making up modern Singapore (Powell, 2020). Mangrove forests constitute 1.1% of Singapore's total land area based on satellite images from 2003 to 2018 (Gaw et al., 2019).

3. Methods

We retrieved core MSBH01B from Marina South (1.27266°N, 103.8653°E) (Fig. 2) through hydraulic piston coring which achieved at least 90% of sediment recovery (Chua et al., 2020). MSBH01B is a continuous ~38.5 m sediment core with surface elevation of 4.1 m mean sea level (MSL) (Chua et al., 2021). The elevation of this core was measured using a Leica System 2000 TCA1800 total station and tied to MSL using tidal information from the nearest tidal station.

Core segments from the MSBH01B were housed in 1 m long stainless-steel core pipes and wax-capped onsite to prevent desiccation and contamination. Core material was removed by a motorized horizontal core extruder and housed in split PVC pipes, wrapped in plastic wrap, and stored at ~4 °C to prevent sample deterioration. Subsequently, core segments were split lengthwise, and one half was immediately stored in D-tubes for archiving (in a cold room at ~4 °C). We subsampled Core MSBH01B at 1 cm intervals between 9.0 and 19.3 m MSL for sedimentological and geochemical analysis.

3.1. Sedimentological analysis

Sedimentological analysis through particle size analysis (PSA) is a fundamental tool for discriminating sedimentary units and interpreting depositional systems (Switzer and Pile, 2015). PSA of sediment samples was undertaken after an initial two-stage pre-treatment of approximately 10 g of sample with 10 *v*/v% hydrochloric acid (HCl) and 15 v/v % hydrogen peroxide (H_2O_2) to remove carbonate and organic matter, and to disassociate clays (Switzer and Pile, 2015). Subsequently, we performed PSA using a Malvern Mastersizer 2000 where samples were first sonicated for 60 s and three replicates averaged (Blott et al., 2004; Ryżak and Bieganowski, 2011). Any samples where the relative standard deviation of the mean grain size values exceeded 5% were re-analysed.

3.2. Carbon isotope and C/N analyses

Carbon isotope analysis provide values that allow for differentiation between terrestrial, riverine, estuarine and marine sediment sources (e.g., Wilson et al., 2005; Lamb et al., 2007). Carbon isotope composition ($\delta^{13}C$) values of −27‰ and less indicate terrestrial-derived (including mangrove-derived) carbon while values greater than −27‰ indicate a marine-derived carbon component (Bouillon et al., 2008).

We sampled bulk sediments from core MSBH01B at 2-cm resolution for stable (organic) carbon isotope analysis following the methodology of Bird et al. (2019). 565 representative aliquots of sediment samples were milled using a mortar and pestle, acidified (HCl conc. 5%) before centrifuging (at least four washes in deionized water) and dried at 60 °C. Approximately 15 mg of sample was weighed and placed in tin capsules before loading onto an autosampling plate. Total organic carbon (TOC) and nitrogen abundances and isotope compositions of the bulk sediments were determined using an elemental analyzer (ECS 4010 CHNSO Analyzer; Costech Analytical Technologies INC, Valencia, CA, USA) fitted with a Costech Zero Blank Autosampler coupled via a ConFloIV to a Thermo Scientific Delta VPLUS using Continuous-Flow Isotope Ratio Mass Spectrometry (EA-IRMS). Calibration curves for elemental abundances were determined for three in-house standards ('High Organic

Carbon', 'Low Organic Carbon' and 'Taipan') within the same analytical sequence, and standard linearity and drift were accounted for in calibration and data reduction calculations. The C/N ratio was determined via weight percentage while $\delta^{13}C$ values are reported as per mille (‰) deviations from the Vee Dee Bee Belemnite (VPDB) reference scale, using the same reference materials as for elemental abundances. Precision for all $\delta^{13}C$ results is ±0.1‰ or better.

3.3. X-ray fluorescence analysis

X-ray fluorescence (XRF) core scanning of marine sediments has been extensively used to study changes in past environmental and climatic processes over a range of timescales (e.g., Haug et al., 2001; Revel et al., 2015). The interpretation of XRF-derived element ratios in paleoenvironmental and paleoclimatic studies primarily considers differences in the relative abundances of particular elements (Rothwell and Croudace, 2015).

Selection of chemical and physical/mechanical weathering proxies require an understanding of the palaeohydrology and source rock mineralogy. Chemical weathering of granite in hot and humid tropical climates is commonly kaolinite [$Al_2Si_2O_5(OH)_4$], a high-alumina clay which can be readily remobilised (Rothwell and Croudace, 2015) and flushed into fluvial channels. The ratio of kaolinite (High Al)/smectite (High Si) is useful as an indicator of chemical weathering which can help identify tropical conditions favouring kaolinite formation (Hu et al., 2013). Aluminium to silica (Al/Si) ratio in the bulk sediment thus reflects the extent of chemical weathering (Rothwell and Croudace, 2015). Sediments and their geochemical signatures from such a low energy coastal environment should therefore provide a reliable of the response of coastal systems to sea-level rise (e.g., Simms and Rodriguez, 2014).

We performed XRF core scanning on core MSBH01B at 1 cm resolution over a 1 cm^2 area (cross-core slit = 10 mm, down-core slit = 10 mm) using an Avaatech XRF Core Scanner II (Richter et al., 2006). Generator settings of 10 kV and 30 kV at 500 maH, and sampling times of 15 s and 25 s respectively, were employed during the scanning of the split core surface. Each core surface was carefully covered with 4 μm SPEXCerti Prep Ultralene® film to prevent desiccation and contamination of the sample and the XRF measurement unit (sensu Tjallingii et al., 2007). Data acquisition was performed by a Canberra X-PIPS Detector (Model SXP 5C-200-1500 V3) with 200 eV X-ray resolution, the Canberra Digital Spectrum Analyzer DAS 1000, and an Oxford Instruments 50 W XTF5011 Rhodium-based X-Ray tube. Data processing was done through analysis of X-ray spectra using WIN AXIL, an Iterative Least square software package (e.g., Kern et al., 2019). Calibration scans were performed daily before and after the XRF-scanning of each core segment to control for equipment drift.

3.4. Radiocarbon dating and age-depth modelling

The radiocarbon dates were previously described in Chua et al. (2021). Briefly, we sampled 16 wood, charcoal, and shell (bivalves and gastropods only) macrofossils for Accelerator Mass Spectrometry (AMS) ^{14}C dating (Baisden et al., 2013). Terrestrial samples were calibrated based on the IntCal20 calibration curve (Reimer et al., 2020). Carbonate samples were calibrated based on the Marine20 calibration curve (Heaton et al., 2020) and corrected for marine reservoir effect using a ΔR value of −235 ± 104 [*deltar* application (Reimer and Reimer, 2017)] using ages derived from paired bivalve and wood samples obtained from the same depth of 14.48 m MSL (Chua et al., 2021).

The 16 AMS ^{14}C ages were used to constrain the age-depth model in this study (Table 1). We used *BChron* (Parnell and Parnell, 2020), an open-source R package utilising a Bayesian statistical approach to establish the chronology for core MSBH01B at cm-scale resolution. Here, 20,000 age-depth realizations were obtained to estimate the median age and 95% confidence intervals at 1 cm resolution.

3.5. Predicting accommodation space (A), sediment supply (S) and palaeowater depths

We apply the *A/S* method (Muto and Steel, 1997) to compare how the interplay between accommodation space and sediment supply relate to transitions in sedimentary units. The *A/S* method predicts that shoreline retreat or retrogradation occurs when $A > S$, while shoreline progradation occurs when $A < S$ (Guerit et al., 2020).

A refers to rate of accommodation creation that is defined as the change in the amount of space, both laterally and vertically, in which minerogenic and organic sediments and materials can accumulate (Rogers, 2021). Singapore is generally tectonically stable, with coastal areas largely flat with uniform topography (Catalao et al., 2020). Accommodation space is thus primarily controlled by relative sea-level changes, with the rate of RSLR and water depths being the proxy for *A*. We estimated RSL and RSLR rates by applying the Error-In-Variables Integrated Gaussian Process (EIV-IGP) model of Cahill et al. (2015) to derive quantitative RSL trends while incorporating vertical and temporal uncertainties of all SLIPs (sea-level index points) from Singapore (Chua et al., 2021). We estimate past water depths by calculating the vertical offset which is the difference between the elevations of the predicted RSL and each dated sample (Bird et al., 2010). We then applied a polynomial regression model to the vertical offset values as well as predicted depth uncertainties to within 95% confidence levels to estimate palaeo water depths with 2 sigma uncertainties.

S refers to the sediment supply primarily controlled by erosion and sediment transport, with the sedimentation rate the proxy for *S*. We used *BChron* (Parnell and Parnell, 2020) to calculate the sedimentation rate for core MSBH01B. Here, 20,000 age-depth realizations were obtained to estimate the sedimentation rate and 95% confidence intervals at 1 cm resolution.

4. Results

4.1. Core description and sedimentology

Holocene sediments from core MSBH01B lie ~13 m below the land surface (surface elevation = 4.1 m). The downcore sedimentology of the Holocene sediments comprise four units, I - IV (Figs. 3 and 4), found between −19.28 m and − 9.00 m MSL. Sediment below the depth of 19.3 m is the Marina South member (MSM) of the Kallang Group (Chua et al., 2020). The MSM primarily comprises subaerially exposed and desiccated marine muds deposited possibly around the Last Interglacial period (Thanh et al., 2021) and serves as a stratigraphic marker for post-LGM Holocene sea-level transgression (Chua et al., 2020).

Unit I (−19.28 m to −18.73 m MSL) is composed of dark brown, organic mud with decomposed macrofossils (i.e., wood, bark and root) and vegetation fragments found abundantly throughout the unit (Fig. 3A). The grain size composition is high in clay and silt, being 28.0 ± 2.0% and 69.7 ± 2.1%, respectively. Sand content is low and variable at 2.4 ± 1.9% (Fig. 4). Pollen analysis (Chua et al., 2021) indicates that Unit I comprises mangrove peat formed in intertidal swamp settings in low-lying river basins and inundated coastal environments.

Unit II (−18.73 m to −12.54 m MSL) is composed of largely homogenous, non-laminated blue grey to grey medium-fine silty mud that contains occasional shells and organic streaks (Fig. 3B and C). Shell occurrence is sporadic and uncommon, although gastropod and bivalve shell preservation is extraordinarily high where found. Unit II is dominated by clay and silt at 30.7 ± 3.5% and 69.1 ± 3.5%, respectively. Sand content is low at 0.2 ± 0.3% (Fig. 4). Foraminiferal analysis (Chua et al., 2021) indicates that Unit II comprises marine muds formed in a shallow sub-tidal marine environment. Shallow benthic species were identified from −13.84 to −12.88 m MSL. The foraminiferal assemblage is dominated by *Elphidium* spp. (47.2 ± 8.7%), *Asterorotalia pulchella* (16.0 ± 7.1%), and *Ammonia* spp. (18.9 ± 4.2%). Foraminifera were absent from −14 m to −19 m MSL (Fig. 4).

Table 1
Carbon isotopic composition ($\delta^{13}C$), total organic carbon (TOC) and carbon-to-nitrogen ratio (C/N) measurements for sedimentary units I – IV in core MSBH01B. Average values and uncertainties are reported at 1 standard deviation (Ave ± 1SD) followed by maximum (Max) and minimum (Min) values, respectively.

Unit	Elevation (m MSL)	$\delta^{13}C$ (Ave ± 1SD)	$\delta^{13}C$ (Max)	$\delta^{13}C$ (Min)	TOC (Ave ± 1SD)	TOC (Max)	TOC (Min)	C/N (Ave ± 1SD)	C/N (Max)	C/N (Min)
Unit I	−19.28 to −18.73	−28.47 ± 0.55	−26.44	−29.01	5.53 ± 1.25	7.79	2.31	39.51 ± 5.22	45.88	25.17
Unit II	−18.72 to −12.54	−26.80 ± 0.54	−25.49	−27.75	1.28 ± 0.21	1.85	0.93	17.88 ± 1.75	24.14	14.52
Unit III	−12.53 to −10.51	−25.84 ± 0.36	−25.18	−26.91	0.98 ± 0.07	1.20	0.80	15.15 ± 0.88	17.30	13.00
Unit IV	−10.50 to −9.00	−26.29 ± 0.54	−25.23	−27.99	1.05 ± 0.20	1.70	0.60	17.59 ± 2.85	28.50	13.80

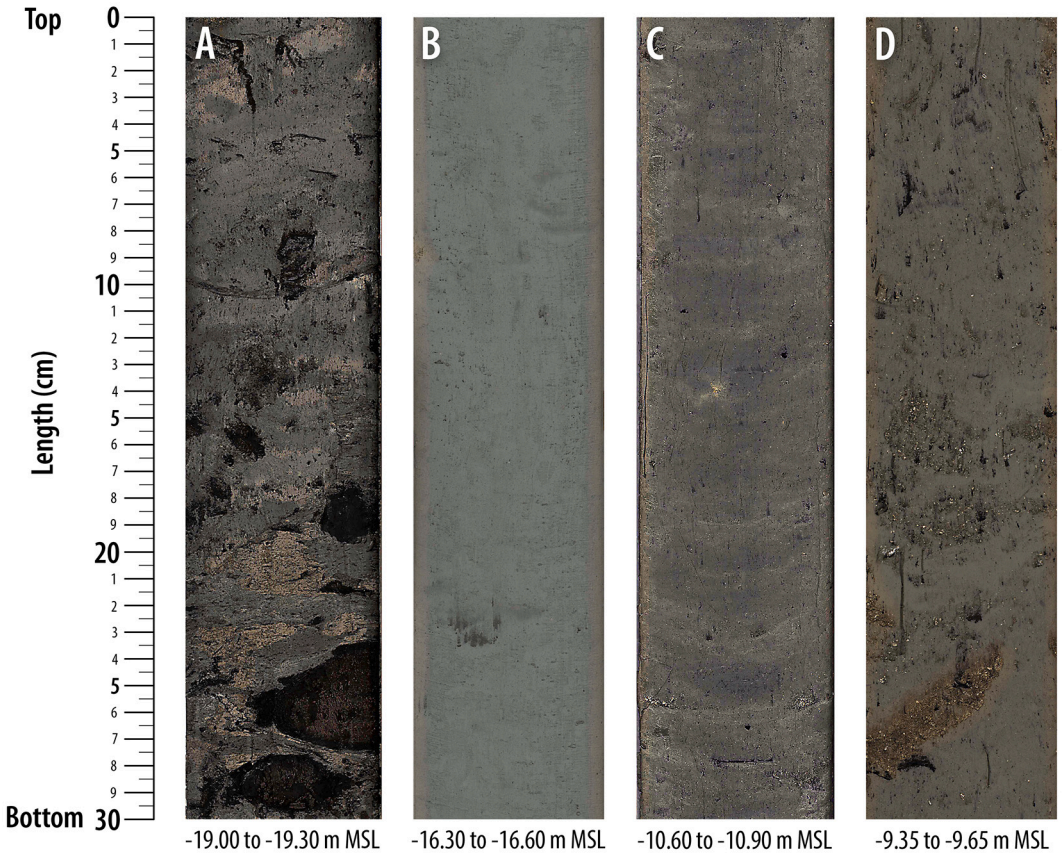

Fig. 3. Selected photographs of sedimentary units from core MSBH01B. Each core stick is 30 cm long. (A) (Unit I: depth in core is −19.00 to −19.30 m MSL): dark brown, organic-rich medium-fine mud with decomposed macrofossils (i.e., wood, bark and root) and vegetation fragments; (B) (Unit II: depth in core is −16.30 to −16.60 m MSL): homogenous, non-laminated greenish grey to grey medium-fine mud that contains occasional shells and organic streaks; (C) (Unit III: depth in core is −10.60 to −10.90 m MSL): blue-dark grey mud with sand with diffused laminations and occasional crushed shell fragments; (D) (Unit IV: depth in core is −9.35 to −9.65 m MSL): dark grey, very poorly sorted, sandy mud with frequent shell and coral fragments. (For interpretation of the references to colour in this figure legend, the reader is referred to the web version of this article.)

Unit III (−12.54 m to −10.51 m MSL) is composed of blue-dark grey medium silty mud with sand, diffused laminations and occasional crushed shell fragments (Fig. 3D). Unit III is slightly coarser grained than Unit II with lower clay and similar silt content at 25.9 ± 1.7% and 69.2 ± 3.5%, respectively. Sand content is variable at 5.0 ± 3.1%. Sand content increases upward, from 1.3% at the base to >10% at the top of the unit (Fig. 4). Foraminiferal analysis published previously (Chua et al., 2021) indicates that Unit III comprise marine muds formed in shallow sub-tidal marine environments. Relative to Unit II, the foraminiferal assemblage is dominated by *Ammonia* spp. (44.0 ± 6.0%), with decreased relative abundance in *Elphidium* spp. (19.3 ± 2.5%) and *Asterorotalia pulchella* (11.2 ± 6.6%) (Fig. 4).

Unit IV (−10.51 m to −9.00 m MSL) is composed of very poorly sorted, medium to coarse dark-grey sandy mud with frequent shell and coral fragments (Fig. 3E). This unit is characterised by a coarsening-upward sequence with increasing frequency of shell and coral fragments, often deposited as lateral beds or within sub-vertical depressions or burrows. Unit IV is coarser grained than Unit III with lower clay and silt content at 22.5 ± 2.4% and 64.0 ± 3.7%, respectively. Sand content is highly variable at 13.5 ± 5.3%. Unit IV coarsens upward with increasing sand content from ~8% at the base to >20% at the top of the unit (Fig. 4). Foraminifera analysis (Chua et al., 2021) indicates that Unit IV comprises marine muds formed in a shallow sub-tidal marine environment. Relative to Unit III, the foraminiferal assemblage is dominated by *Asterorotalia pulchella* (28.7 ± 6.0%), *Ammonia* spp. (22.5 ± 11.6%) and *Textularia* spp. (12.6 ± 6.0%) (Fig. 4).

4.2. Geochemical analysis

$\delta^{13}C$ and C/N values show variability (Table 1; Fig. 4) generally coincident with the transitions in sedimentary units identified above (Refer to Table S1 in the supplementary file for further details).

The $\delta^{13}C$ value in Unit I is low, and TOC and C/N ratio values are both high relative to the other overlying sedimentary units (Table 1).

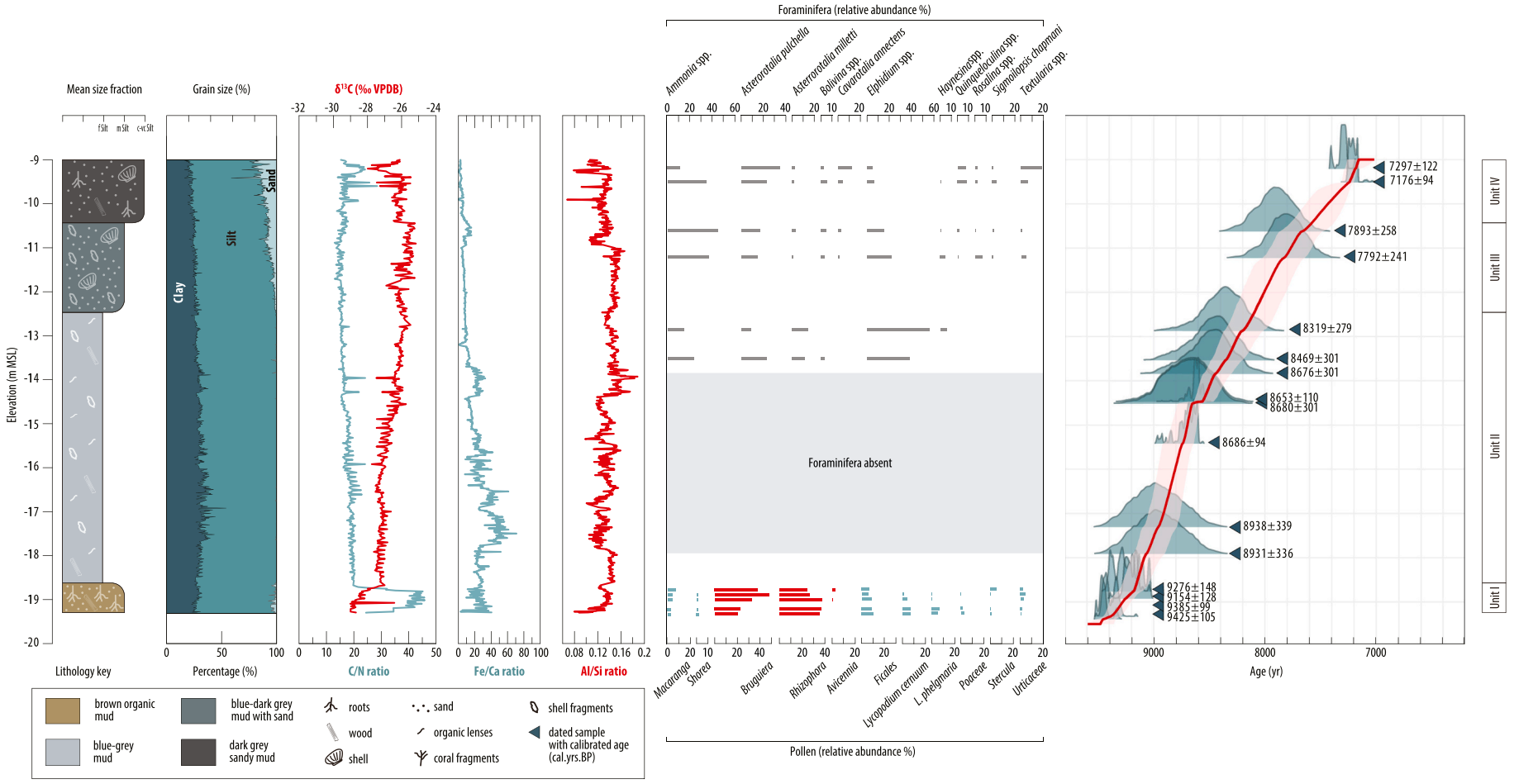

Fig. 4. Lithology and geochemistry of core MSBH01B with mean size fraction, grain-size, $\delta^{13}C$ and C/N ratio, XRF elemental ratios of Fe/Ca and Al/Si and relative foraminiferal and pollen abundances shown. Relative foraminiferal abundances (genera/species abundance >2%) are shown corresponding to dated horizons. Relative pollen abundances are shown for mangrove (red bars) and non-mangrove (teal bars) species. Age-depth model (*BChron*) is shown with calibrated ^{14}C ages corresponding to depths of dated samples. (For interpretation of the references to colour in this figure legend, the reader is referred to the web version of this article.)

Table 2
Iron-calcium (Fe/Ca) and aluminium-silica (Al/Si) elemental ratios from X-Ray Fluorescence (XRF) scanning of sedimentary units I – IV in core MSBH01B. Average values and uncertainties are reported at 1 standard deviation (Ave ± 1SD) followed by maximum (Max) and minimum (Min) values, respectively.

Unit	Elevation (m MSL)	Fe/Ca (Ave ± 1SD)	Fe/Ca (Max)	Fe/Ca (Min)	Al/Si (Ave ± 1SD)	Al/Si (Max)	Al/Si (Min)
Unit I	−19.28 to −18.73	24.16 ± 8.01	40.68	2.51	0.13 ± 0.01	0.15	0.08
Unit II	−18.72 to −12.54	24.57 ± 12.58	70.97	0.96	0.14 ± 0.01	0.19	0.10
Unit III	−12.53 to −10.51	7.74 ± 2.44	15.92	3.15	0.14 ± 0.01	0.17	0.11
Unit IV	−10.50 to −9.00	4.22 ± 2.60	12.90	0.24	0.13 ± 0.01	0.14	0.07

The $\delta^{13}C$ value in Unit II increases upcore from −27.5 ‰ at the base to −25.9 ‰ at the top of the unit. TOC and C/N in Unit II both decreased compared to Unit I (Table 1). The $\delta^{13}C$ value in Unit III is highest in the core with −26.0 ‰ at the base to −25.3 ‰ at the top of the unit. TOC and C/N remained low and further decreased compared to Unit II (Table 1). The $\delta^{13}C$ value in Unit IV is highly variable, punctuated by peak values of −27.28 ‰ at −9.59 m MSL, −27.46 ‰ at −9.51 m MSL and 27.99 ‰ at −9.20 m MSL (Fig. 4). TOC and C/N in Unit IV increased slightly compared to Unit III but remained low (Table 1).

4.3. Geochemical analysis (XRF elemental ratios)

Elemental ratios, namely Fe/Ca and Al/Si, show variations (Table 2; Fig. 4) coincident with transitions in sedimentary units identified above (Refer to Table S1 in the supplementary file for further details).

Fe/Ca is low and variable in Unit I. Fe/Ca then increases to peak values near the base of Unit II before decreasing upcore. Fe/Ca from Unit III is generally low, albeit with a small peak of 15.9 at −10.72 m MSL. Fe/Ca from Unit V decreases further to ~2.0 at the top of the unit.

Al/Si is highly variable from Unit I to Unit IV but average values stay within a narrow range (Table 2). Generally Al/Si increases to a peak value of 0.19 at −13.93 m MSL before decreasing to minimum values of ~0.7 within Unit IV.

4.4. Chronology and age-depth modelling

We obtained 16 radiocarbon ages from charcoal, wood and shell material from −19.39 m to the top of the core at −9.21 m MSL (Chua et al., 2021) ranging from 9500 to 7200 cal. yr. BP. Fig. 4 shows the age-depth model developed by *BChron* for each identified sedimentary unit. Unit I is constrained by 4 dates between 9425 ± 105 and 9276 ± 148 cal. yr. BP, and deposited from 9500 to 9200 cal. yr. BP. Unit II is constrained by 8 dates between 8931 ± 336 and 8319 ± 279 cal. yr. BP, and deposited from 9200 to 8200 cal. yr. BP. Unit III is constrained by 2 dates of 7893 ± 258 and 7792 ± 241 cal. yr. BP and deposited from 8200 to 7600 cal. yr. BP. Unit IV is constrained by 2 dates of 7297 ± 122 and 7176 ± 94 cal. yr. BP and deposited from 7600 to 7200 cal. yr. BP.

4.5. Predicting accommodation space (A), sediment supply (S) and palaeo water depths

Holocene sea level rose rapidly from −21.0 m to −0.7 m from ~9.5 to 7.2 cal. ka BP (Chua et al., 2021). RSLR rates rose to maximum values of 14.5 ± 2.2 mm/yr at 9.0 cal. ka BP and gradually decelerated to 3.1 ± 1.8 mm/yr by 7.2 cal. ka BP.

Outputs from *BChron* (Fig. 4) show that average sedimentation rate was relatively constant throughout the core. Modelled sedimentation was 2.7 ± 0.4 mm/yr from ~9.3 ka to ~8.6 cal. ka BP increasing to 4.1 ± 0.7 mm/yr from ~8.6 ka to ~7.2 cal. ka BP (Fig. 4).

RSLR rates (*A*) from 9.5 to 9.2 cal. ka BP were up to 12.5 ± 2.9 mm/yr against a background sedimentation rate (*S*) of 2.5 mm/yr (Fig. 5). Average A/S value was 5.1 ± 0.3 and average water depth was ~ − 0.8 ± 1.3 m.

RSLR rates (*A*) from 9.2 to 8.8 cal. ka BP were up to maximum values of 14.5 ± 2.2 mm/yr against sedimentation rate (*S*) of 5 mm/yr (Fig. 5). Average A/S value was 3.1 ± 0.8. Water depth increased rapidly from −0.1 ± 1.4 m to 2.5 ± 1.5 m with an average depth of −1.2 ± 1.6 m.

RSLR rates (*A*) from 8.8 to 8.2 cal. ka BP was marked by high but decelerating sea-level rise rates from 13.6 ± 2.0 mm/yr at 8.8 cal. ka BP to ~6.8 ± 1.5 mm/yr by 8.2 cal. ka BP (Fig. 5A) against sedimentation rate *(S)* from 5 mm/yr at 8.8 cal. ka BP to 3 mm/yr by 8.2 cal. ka BP, punctuated by an abrupt decrease in sedimentation rate (*S*) to minimal values as low as 0.5 mm/yr between 8.7 and 8.5 cal. ka BP. Average A/S value was 4.6 ± 5.2, punctuated by an abrupt peak of 21.8 at 8.6 cal. ka BP. Water depths increased rapidly from 2.5 ± 1.5 m to 5.2 ± 1.2 m with an average depth of 4.1 ± 1.4 m.

RSLR rates (*A*) from 8.2 to 7.6 cal. ka BP was coincident with low and decelerating rates of sea-level rise from 6.7 ± 1.5 mm/yr to 3.7 ± 1.5 mm/yr (Fig. 5A) with sedimentation rates (*S*) decreasing from between 3.3 and 2 mm /yr (Fig. 5A). Average A/S value was 1.7 ± 0.2. Water depths generally plateaued with an average of ~5.6 ± 0.2 m (subtidal).

RSLR rates (*A*) from 7.6 to 7.2 cal. ka BP was coincident with low and stable rates of sea-level rise from 3.7 ± 1.5 mm/yr to 3.1 ± 1.8 mm/yr (Fig. 5A) with sedimentation rates (*S*) at a consistent rate of 2 mm /yr (Fig. 5A). Average A/S value remained constant at 1.7 ± 0.2. Water depths generally plateaued with an average of ~5.9 ± 0.2 m (subtidal).

5. Discussion

Integration of sea level and sedimentation rate change, sedimentological and geochemical records of sediment core MSBH01B reveals a sequence of coastal responses to early-mid Holocene sea-level rise at Marina South (Fig. 6). The sedimentary succession for MSBH01B comprise of a highly organic sandy-silt base layer overlain by a classical coarsening-upward sequence We present a multi-proxy approach to identify five depositional phases between 9.5 cal. ka BP and 7.2 cal. ka BP (Fig. 5).

5.1. Phase 1: 9.5–9.2 cal. ka BP [Coastal mangrove forest]

Coastal mangroves inhabited this site from 9.5 to 9.2 cal. ka BP (Chua et al., 2020) (Fig. 6A), evidenced by >40% relative abundance of mangrove pollen found within the organic-rich peaty sediment unit (Chua et al., 2021). These mangroves were rapidly inundated due to rapid RSLR (Fig. 5A) with A/S values of 5.1 ± 0.3 which led to mangroves disappearing at the Marina South coring location within 300 years. Incursions of tidal sands also gradually decreased (Fig. 5B) as the coastal system migrated landwards.

The rapid marine inundation during this time period is supported by a 2 ‰ increase in $\delta^{13}C$ from ~ − 29.0 ‰ VPDB (highly terrestrial) to ~ − 27.1 ‰ VPDB indicating a progressively increasing marine influence (Fig. 5C). Such values agree with other tropical mangrove and estuarine/shallow marine samples from Singapore (Bird et al., 2010) and the Pearl River delta (Yu et al., 2010). The coeval decrease in C/N also suggests that the mangrove system, characterised by low $\delta^{13}C$ (<~ − 27.1 ‰) and high C/N (>20) values, was transitioning to an estuarine islet mangrove system where C/N decreases due to a higher proportion of marine phytoplankton (Tue et al., 2020). The relatively high Fe/Ca values (Fig. 5D) is expected for this intertidal mangrove environment where inland terrestrial input from surface water flow through tidal and

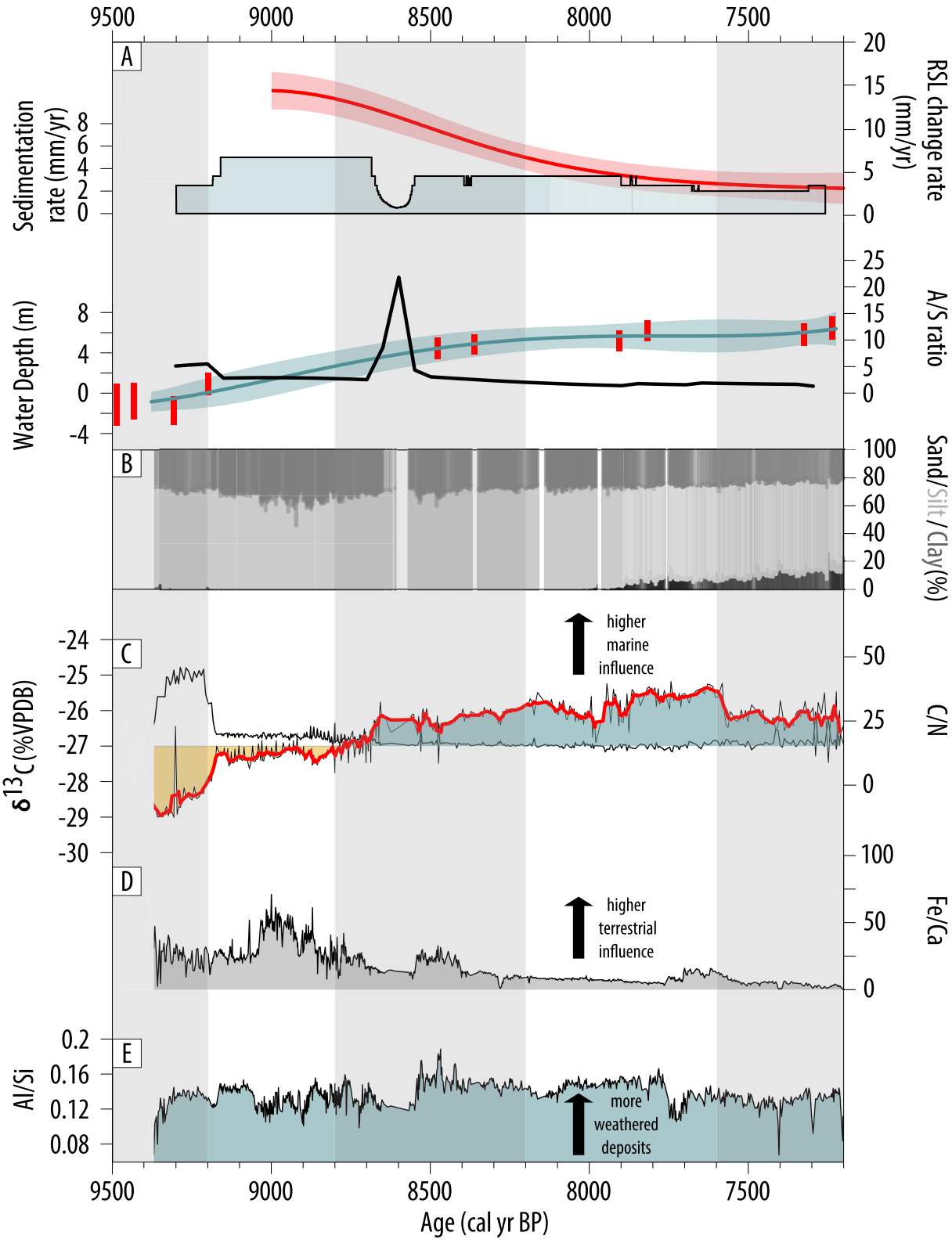

Fig. 5. Stacked sediment and geochemical proxy records during the early to mid-Holocene (9.5–7.2 cal. ka BP). (A) Stacked records of RSL change rate represented by red line (mean) and pink band (2 sigma uncertainty) from Chua et al. (2021), sedimentation rate (teal bar graph) generated by *BChron*, A/S ratio (black line) and estimated water depth represented by dark teal (mean) and light teal band (95% confidence). Red bars represent full vertical uncertainty of each sea-level data point from MSBH01B. (B) Stacked grain size percentages of clay (mid grey), silt (light grey) and sand (dark grey). (C) Juxtaposed $\delta^{13}C$ record and weighted average values represented as black line with overlapping bold red line, respectively, and C/N ratio as thin black line. -27 ‰ used as threshold value delineating marine (> − 27 ‰ in teal) and terrestrial (<−27 ‰ in dull yellow) influence. (D) Fe/Ca plot which indicates relative terrestrial (Fe) to marine (Ca) influence. (E) Al/Si plot which indicates degree of weathering in deposited sediments. (For interpretation of the references to colour in this figure legend, the reader is referred to the web version of this article.)

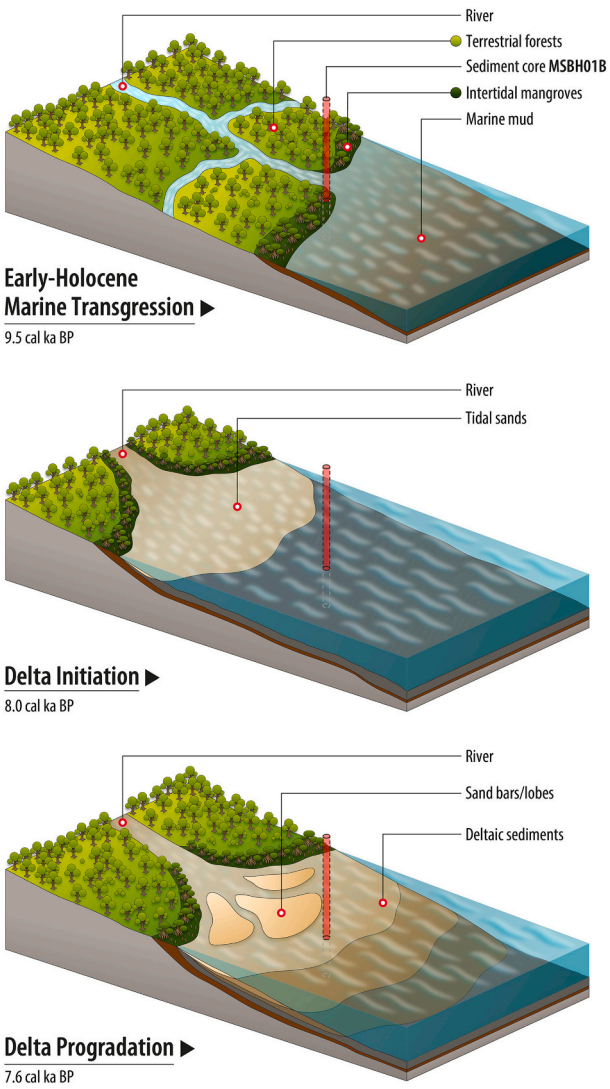

Fig. 6. Time-stepped evolution model of the Kallang River Basin coastal area (not to scale). Red cylinder denotes location of core MSBH01B. (A) coastal mangroves during a period of high sea-level rise rates (marine transgression) coupled with low sedimentation rates (A/S = 5.1 ± 0.3); (B) subaqueous delta front aggrading vertically (delta initiation) during a period of low and stable sea-level rise rates coupled with similar sedimentation rates (A/S = 1.7 ± 0.2); (C) Deltaic lobes and sandy mudflats prograding seaward (delta progradation) during a period of lowest and stable sea-level rise rates coupled with similar sedimentation rates (A/S = 1.7 ± 0.2). (For interpretation of the references to colour in this figure legend, the reader is referred to the web version of this article.)

fluvial channels can be significant (e.g., Alongi and Brinkman, 2011; Pérez et al., 2017). The increase in Al/Si (Fig. 5E) could be due to a decrease in quartz-rich tidal sands as the coastline retreated landward turning the intertidal environment to a more sub-tidal/brackish one.

Mangrove ecosystems have been promoted as coastal defences against storms and sea level change due to their resilience and ability to vertically 'keep pace' with rising seas (e.g., Alongi, 2008; Lovelock et al., 2015). However, the local disappearance of mangroves at Marina South within ~300 years highlights the need to investigate thresholds and tipping points of mangroves to sustainably trap sediment and keep pace with sea-level rise. Saintilan et al. (2020) calculated a sea-level rise rate of 7 mm/yr as the threshold level for sustained mangrove vertical sedimentation in farfield regions during the Holocene. Similarly, early Holocene wetland submergence and retreat threshold levels were calculated at 6–9 mm/yr for the Mississippi delta (Törnqvist et al., 2021). The vertical sedimentation rate of the Marina South coastal mangrove system was estimated at ~2.5 mm/yr and thus could not keep pace with the ~15 mm/yr sea level rise. The mangrove system either experienced dieback after more permanent inundation or migrated landward assuming landward conditions are viable and available for mangrove growth (Di Nitto et al., 2014; Woodroffe et al., 2016).

5.2. Phase 2: 9.2–8.8 cal. ka BP [Coastal plain estuary]

The mangrove forest was succeeded by a lower energy estuarine environment with average A/S values of 3.1 ± 0.8. This is supported by an increase in clay content due to flocculation (Winterwerp, 2002) amidst sustained rapid RSLR. Foraminifera are absent in this unit (Fig. 4) potentially due to taphonomic alteration through acidic dissolution of calcareous tests which is a common occurrence in other estuarine sediment archives (e.g., Horton et al., 2005; Berkeley et al., 2007).

The geochemistry reveals consistently low $\delta^{13}C$ values and peak Fe/Ca values, particularly from ~9.1 ka to 8.9 cal. ka BP, suggesting strong fluvial discharge of terrigenous material (Rothwell and Croudace, 2015) into possibly river-dominated estuarine conditions. Such borderline terrestrial signals of ~27 ‰ and elevated C/N values of ~20 (Fig. 5C) agree well with other Holocene estuarine studies with similar $\delta^{13}C$ values between −31‰ to −27‰ and C/N values from ~12–30 (e.g., Wilson et al., 2005; Khan et al., 2015b).

The latter half of this estuarine phase commencing from ~9 cal. ka BP is marked by increasing marine influence supported by a sharp decrease in Fe/Ca and lower Al/Si values (Fig. 5D and E). This is coincident with a period of higher clay content (~5% increase) from 8.9 ka to 8.8 cal. ka BP (Fig. 5B) suggesting decreasing amounts of coarser weathered terrigenous material reaching Marina South. This trend could be explained by dominant deposition of marine muds relative to terrigenous deposits (Leonardi et al., 2021) due to backstepping of coastal morphologies and deposition of coarser terrigenous material further inland.

Such rapid landward retrograde events during the early Holocene by estuarine environments have been recorded elsewhere. For example, estuaries along the tropical Gulf of Mexico record rapid retrogradation at ~8.2 cal. ka BP accompanied by rapid flooding of the sub-aerial delta plain (Rodriguez et al., 2010). The Shoalhaven coastal plain in southeast Australia was fully inundated by ~8.5 cal. ka BP and the estuary reached its maximum retreat extent by 7.5 cal. ka BP (Carvalho and Woodroffe, 2020). In Asia, estuarine back-stepping events were identified at ~8.5 cal. ka BP at the three river systems, namely the Chang Jiang (China), Song Hong (Vietnam) and Kiso (Japan) (Hori and Saito, 2007). Together with the Kallang River Basin, these sites are all incised valley-fill systems nested in low-gradient coastal plains, indicating that localised antecedent topography is a significant factor dictating the behaviour of coastal retreat in a RSLR scenario.

5.3. Phase 3: 8.8–8.2 cal. ka BP [Prodelta]

Prodelta muds succeeded the estuarine muds from 8.8 to 8.2 cal. ka BP with an average A/S value of 4.6 ± 5.2. We postulate a rapid backstepping of the system, resulting in formation of a highly landward bayhead delta fronted by these prodelta muds which typically forms furthest offshore (Dladla et al., 2021), This process is supported by the abrupt A/S peak of 21.8 caused by decelerating RSLR and low gradient topography (Fig. 5A) which resulted in continued landward advance of the coastline but allowed deposition of distal subtidal prodelta marine muds at the core location. The foraminiferal assemblage observed in Unit II is comparable to modern subtidal assemblages found at the shallow (< 20 m), eastern coast of Johor, Malaysia (Minhat et al., 2016).

The rapidly increasing $\delta^{13}C$ values from −27 ‰ to −26 ‰ and low and stable C/N values of ~15 (Fig. 5C) indicate stronger marine influence with greater phytoplankton abundance (Lamb et al., 2007; Wilson, 2017) as prodelta conditions gradually dominated. Fe/Ca values

continue to decrease between 8.8 and 8.5 cal. ka BP (Fig. 5D) which suggest decreasing terrestrial influence as the tidal frame moved landward. Coincident reduction in Al/Si (Fig. 5E) indicates less weathered fluvial sediment being deposited resulting in the abrupt decrease in sedimentation rate between 8.7 and 8.5 cal. ka BP. This increase in marine inundation should result in continued decrease in Fe/Ca and Al/Si. However, Fe/Ca and Al/Si unexpectedly increased from 8.5 cal. ka BP to 8.4 cal. ka BP. We thus postulate that climate exerted a stronger influence on geochemical signals during this phase of decelerating sea-level rise. These geochemical trends may represent a drier phase from 8.8 cal. ka BP to 8.5 cal. ka BP followed by a wetter phase from 8.5 cal. ka BP to ~8.2 cal. ka BP. This postulated wetter phase is coincident with prominent peaks in clay content at 8.5 cal. ka BP (~37.9%) and 8.4 cal. ka BP (~40.2%) (Fig. 5B) which could be caused by higher precipitation and weathering rates bringing more iron- and alumina-rich weathered clays from inland sources, supported by coincident Fe/Ca and Al/Si peaks representing pulses of higher terrigenous input. A proximal oxygen isotope record from the Tangga cave in Sumatra supports this dry-wet phase postulation between 8.8 cal. ka BP and 8.2 cal. ka BP (Wurtzel et al., 2018). This speleothem-derived $\delta^{18}O$ record similarly shows an enrichment of $\delta^{18}O$ from −8.5 ‰ to −7.5 ‰ between 8.8 cal. ka BP and 8.5 cal. ka BP indicating lower precipitation, followed by higher precipitation by 8.2 cal. ka BP.

The most prominent climate event during this time period is the 8.2 ka event (Barber et al., 1999). We do not observe clear evidence pointing to climatic shifts associated with the 8.2 ka climate event, nor clear sedimentological features linked to a sea-level pulse due to catastrophic drainage from proglacial Lake Agassiz-Ojibway between 8.6 ka and 8.4 cal. ka BP (e.g., Cronin et al., 2007; Hijma and Cohen, 2010). Our current sediment record lacks the necessary resolution and source-to-sink precision to fingerprint this short-lived, and spatially and temporally variable climate event (Morrill and Jacobsen, 2005; Thomas et al., 2007).

5.4. Phase 4: 8.2 ka – 7.6 cal. ka BP [Delta Front]

Shelly upward-coarsening delta front deposits overlaid the prodelta muds as A/S decreases to 1.7 ± 0.2 (Fig. 5B) through high bedload deposition which commonly dominates the subtidal zone. The delta front typically sits landward of the prodelta and forms proximal to channel mouths where reduction of flow velocities results in deposition of coarser material (Fig. 5B). The foraminiferal assemblages observed in Unit III is comparable to modern subtidal assemblages found at the eastern coast of Johor, Malaysia (Minhat et al., 2016). The shift in dominance from *Elphidium* to *Ammonia* spp. in the transition from Unit II to III suggests a deepening of coastal waters coupled with decreased brackishness (Suriadi et al., 2019).

We expect the $\delta^{13}C$ values to continue increasing indicating higher marine influence against a background of low but consistent sea-level rise. However, we observe gradually decreasing $\delta^{13}C$ values from −25.5 ‰ to ~ − 27 ‰ from 8.2 ka to 8 cal. ka BP, before a reversal to maximum $\delta^{13}C$ values of ~25 ‰ by 7.6 cal. ka BP (Fig. 5C). This is not erroneous, as we observe congruence with the Bird et al. (2010) Geylang core record which shows a similar coeval 1 ‰ depletion in $\delta^{13}C$ values. This reversal could also be explained by climate as the dominant driver instead of sea-level rise, i.e., increased precipitation bringing more terrigenous inputs associated with increased fluvial discharge (Yu et al., 2011). The Tangga cave speleothem record likewise shows a coeval decrease in $\delta^{18}O$ value of ~0.5 ‰ indicating higher precipitation (Wurtzel et al., 2018). $\delta^{13}C$ value in the core subsequently increased from −27 ‰ at 8 cal. ka BP to ~ − 25 ‰ by 7.6 cal. ka BP (Fig. 5C), congruent with a coeval ~1 ‰ $\delta^{13}C$ increase in the Geylang core (Bird et al., 2010), which might represent a return to more dominant marine conditions. Bird et al. (2007, 2010) suggested that RSLR during this time period was punctuated by a 400-year near cessation in SLR rate centred at 7.6 cal. ka BP before increasing thereafter. However, Lambeck et al. (2014) showed continued RSLR globally during this time period suggesting more localised drivers. The sudden (1 ‰) and sustained depletion $\delta^{13}C$ at 7.6 cal. ka BP could also be explained by a localised geomorphological shift due to deposition of predominantly terrestrial-derived carbon rather than an oscillation in relative sea level. Furthermore, the new Singapore sea-level record comprising re-evaluated sea-level data could not verify the presence of this RSL inflection centred at 7.6 cal. ka BP (Chua et al., 2021).

Generally low and stable Fe/Ca values (Fig. 5D) during this time period likewise reflects the continued decreasing terrestrial / increasing marine influence resulting from the interplay between proportionately less iron-rich hinterland sediments, or more marine-sourced calcium, being deposited. Coeval increasing Al/Si values (Fig. 5E) indicate a high degree of weathered material deposited from 8.0 cal. ka BP to 7.7 cal. ka BP, presumably associated with a period of high precipitation (Wurtzel et al., 2018). However, divergent Fe/Ca and Al/Si trends are observed from 7.8 cal. ka BP to 7.6 cal. ka BP, expressed as an abrupt reduction in Al/Si coincident with a slight increase in Fe/Ca. One possible reason is that clay-rich delta front sediments, although sensitive to climate, could lag climate shifts up to the order of millennium (Thiry, 2000). This abrupt decrease in Al/Si could thus be a lagged response to the drying phase from 8.0 cal. ka BP to 7.7 cal. ka BP (Wurtzel et al., 2018) where weathering weakened in line with weaker monsoons (Hu et al., 2013). Another more likely reason is spatially variable deposition rather than changes in provenance or climate-related drivers and represents the transition to coarser deltaic morphologies. This could be explained by preferential deposition of coarser, less weathered terrigenous sediments (High Fe, Low Al input) at Marina South, and bypassing of finer, more weathered sediments which were deposited further seaward (e.g., McSweeney et al., 2021) and hence distal from core location.

This timing between 8.0 cal. ka BP and 7.6 cal. ka BP potentially marked the delta initiation phase of the Kallang River coast (Fig. 6B). There is some temporal variability between delta initiation timings of major river systems in Southeast Asia: the Red River Delta in Vietnam (9.0 cal. ka BP – 8.5 cal. ka BP) (Tanabe, 2003; Hori et al., 2004; Hori and Saito, 2007), Mekong Delta (8.0 cal. ka BP) (Tamura et al., 2009; Nguyen et al., 2010; Hanebuth et al., 2012) and the Chao Phraya in Thailand (8.0 cal. ka BP – 7.0 cal. ka BP) (Tanabe et al., 2003). The difference in timing could be due to spatial variability in Glacial Isostatic Adjustment (GIA) response and hence temporal variability in Holocene relative sea-level change (i.e., deceleration and stillstand) within the inner Sunda shelf (e.g., Bradley et al., 2016; Chua et al., 2021).

5.5. Phase 5: 7.6 ka – 7.2 cal. ka BP [Delta formation and seaward progradation]

Coarser sandy delta deposits overlay the delta front silts from 7.6 to 7.2 cal. ka BP with average A/S value of 1.7 ± 0.2 coincident with low and stable rates of sea-level rise (Fig. 5). Sediments continue to coarsen-upward with increased shell, coral and infilled burrows, features commonly found in such delta deposits. We observe a plateau in estimated water depth (Fig. 5A) rather than a shallowing-up pattern typical of delta successions distal from the equator (e.g., Hori and Saito, 2007). Equatorial deltas are largely subaqueous, including the Mahakam Delta in Eastern Borneo (e.g., Storms et al., 2005) and the Amazon Delta in Brazil (e.g., Kuehl et al., 1986), and grow laterally seaward. We postulate that continued bypassing of river bedload restricted vertical growth at the core location but sediments were synchronously deposited further offshore. The assemblage in Unit IV displays higher species diversity and comprise species commonly recovered from subtidal to shallow marine sediments in the coastal waters off Johor (Minhat et al., 2016).

An abrupt decrease of ~1 ‰ in $\delta^{13}C$ value at 7.6 cal. ka BP and a subsequent sustained decrease, coupled with generally stable C/N values (Fig. 5C), suggest increasing terrestrial influence. However, the decrease in Fe/Ca and Al/Si (Fig. 5D and E) indicate reduced terrestrial influence that contradicts the $\delta^{13}C$ signal. This can be explained by

coeval changes in geomorphology, topography and fluvial energy gradient. Given the rapid basin infilling and continued aggradation of the delta front in the preceding time period, we propose these decreases in Fe/Ca and Al/Si are due to a combination of (1) inadequate accommodation space and resultant basin sedimentation bypass leading to more seaward sediment delivery (e.g., McSweeney et al., 2021), and (2) proportionately increased contribution by marine sources which can support accretion of tidal flats (Leonardi et al., 2021). This second mechanism is supported by consistently low Fe/Ca values due to high biogenic carbonate contribution in the shallow marine environment, coupled with lesser detrital material (Fe) from terrestrial sources.

The delta initiation process of the Kallang River Basin commenced through initial aggradation (by ~8.0 cal. ka BP), followed by progradational stacking and delta growth as seaward advance became dominant after 7.6 cal. ka BP (Fig. 6C). This agrees well with other delta growth chronologies (e.g., Hori and Saito, 2007; Tamura et al., 2009; Hanebuth et al., 2012) where favourable conditions were created due to decelerating sea-level rise (Stanley and Warne, 1994). Many major river deltas experienced early growth between 8.0 ka and 6.0 cal. ka BP due to RSL slowdown or even stillstands in Asia, including the Mekong (e.g., Tamura et al., 2009; Nguyen et al., 2010; Hanebuth et al., 2012), the Pearl River (e.g., Zong et al., 2012), and the Yangtze (e.g., Hori and Saito, 2007; Wang et al., 2012). Similarly, the Mississippi Delta experienced rapid seaward progradation at ~7.0 cal. ka BP only when sea-level rise decelerated to <3 mm/yr (Törnqvist et al., 2021).

This study produces an A/S value of 1.7, producing the first estimated threshold value at which the southern coast of Singapore switched from retrogradation to aggradation/progradation phases during the early-mid Holocene. Constraining the threshold or the tipping point that switches coastal retreat to either delta initiation and/or coastal progradation is important for predicting and hence mitigating future coastal response to sea-level rise under a variety of warming scenarios (e.g., Syvitski et al., 2009; Tessler et al., 2018). This threshold value translates to a ~ 3 mm/yr difference between sea-level rise and sedimentation rate which is similar to modern sea-level rise rates of 3.7 mm/yr (Fox-Kemper et al., 2021) coupled with greatly reduced sediment supply or subsidence due to anthropogenic pressures driving retrogradation of modern deltas (Nienhuis and van de Wal, 2021). Deltas today face pressures such as sediment reduction due to urbanisation (e.g., concretisation of riverbanks) and upriver damming. For example, the Yangtze delta retrograded substantially since the 1980s due to significant reduction in sediment supply (Zhan et al., 2020) which led to reversal from net accretion to net erosion of the main Yangtze mouth bar and prodelta since 2007 (Luan et al., 2021). Delta retrogradation can be further exacerbated by coastal subsidence due to freshwater extraction and compaction by overburden (Haque and Hoyanagi, 2021). For example, the Chao Phraya Delta has retreated up to 10 m/yr over the last 60 years primarily driven by groundwater withdrawal causing >90 cm subsidence against a backdrop of modern sea-level rise (Bidorn et al., 2021).

6. Conclusion

We present the coastal response to early to mid-Holocene sea-level change from the Kallang River, Singapore, based on high-resolution sedimentological and geochemical results from sediment core MSBH01B.

We identify five depositional phases between 9.5 cal. ka BP and 7.2 cal. ka BP:

(1) coastal mangrove peaty muds deposited during a period of rates of high sea-level rise rates coupled with low sedimentation rates (A/S = 5.1 ± 0.3) (9.5–9.2 cal. ka BP);
(2) estuarine muds deposited as the coastline retreated during a period of high sea-level rise rates coupled with high sedimentation rates (A/S = 3.1 ± 0.8) as the coastline became more permanently inundated (9.2–8.8 cal. ka BP);
(3) pro-delta muds deposited during a period of high but decreasing sea-level rise rates coupled with low sedimentation rates (A/S = 4.6 ± 5.2) as coastline retreat slowed down (8.8–8.2 cal. ka BP);
(4) coarser subaqueous delta front mud with sand aggrading vertically during a period of low and stable sea-level rise rates coupled with equivalent sedimentation rates (A/S = 1.7 ± 0.2) (8.2–7.6 cal. ka BP);
(5) coarse deltaic sandy muds prograding seaward during a period of lowest and stable sea-level rise rates coupled with equivalent sedimentation rates (A/S = 1.7 ± 0.2) (7.6–7.2 cal. ka BP).

This study provides a case study for tropical estuarine-deltas coastal systems in response to a variety of sea-level rise scenarios, and is of critical importance for the densely populated coastal regions of Southeast Asia. The new statistically robust Holocene sea-level record (Chua et al., 2021) and high-resolution, multiproxy analysis of sediment core MSBH01B allowed for a detailed study of sea-level rise and sedimentation rates as key drivers for coastal changes during the early-mid Holocene. Climate (precipitation) changes did not significantly impact timing of coastal change, but rather drove spatial variability in deposition patterns of terrigenous sediment. Our results provide a natural baseline rate of change that will be exceeded with anthropogenic climate change induced sea-level rise, with modern rates already reaching early-mid Holocene rates of up to 3.7 mm/yr (Fox-Kemper et al., 2021). This study provides an estimated threshold A/S value of 1.7 for coastal retreat to be utilised in adaptation scenarios against sea-level and climate change, and mitigate coastal vulnerabilities exacerbated by sediment deficit, nearshore erosion and urban encroachment on coastal zones which threaten Singapore. This study also provides a simple methodology for coastal scientists to obtain local threshold values of other equatorial cities built on floodplains and deltas in order to adapt and/or mitigate effectively against 21st century SLR.

Declaration of Competing Interest

The authors declare the following financial interests/personal relationships which may be considered as potential competing interests:

Stephen Chua, Adam Switzer, Benjamin Horton reports financial support was provided by Government of Singapore Ministry of Education. Stephen Chua reports financial support and travel were provided by Australian Government (Endeavour Research Fellowship).

Acknowledgements

The authors would like to thank Muhammad Hadi Ikhsan for producing the figures and schematics for this paper. We are grateful to the journal editor-in-chief Edward Anthony and three anonymous reviewers for their valuable comments which improved the manuscript. The authors have no financial or conflict of interest to report. This research is conducted in part using the research facilities at the Advanced Analytical Centre in James Cook University, Cairns, Australia supported by an Endeavour Research Fellowship from the Australian Government awarded to SC in 2017. This article is a contribution to IGCP Project 725 “Forecasting Coastal Change”. This work comprises Earth Observatory of Singapore contribution no. 481.

This research was supported by the Earth Observatory of Singapore (EOS) grants M4430132.B50-2014 (Singapore Quaternary Geology), M4430139.B50-2015 (Singapore Holocene Sea Level), M4430188.B50-2016 (Singapore Drilling Project), M4430245.B50-2017 and M4430245.B50-2018 (Kallang Basin Project). SC, ADS, and BPH are supported by the Singapore Ministry of Education Academic Research Fund MOE2019-T3-1-004 and MOE2018-T2-1-030, the National Research Foundation Singapore, the Singapore Ministry of Education under the Research Centers of Excellence initiative, and by the Nanyang Technological University. Any opinions, findings and conclusions or recommendations expressed in this material are those of the author(s)

and do not reflect the views of the National Research Foundation, Singapore, and the National Environment Agency, Singapore.

The data that support the findings of this study are openly available in NTU research data repository DR-NTU (Data) at https://doi.org/10.21979/N9/UHXWSJ

Appendix A. Supplementary data

Supplementary data to this article can be found online at https://doi.org/10.1016/j.margeo.2023.107146.

References

Alongi, D.M., 2008. Mangrove forests: Resilience, protection from tsunamis, and responses to global climate change. Estuarine. Coast. Shelf Sci. 76, 1–13.

Alongi, D.M., Brinkman, R., 2011. Hydrology and Biogeochemistry of Mangrove Forests. In: Levia, D.F., Carlyle-Moses, D., Tanaka, T. (Eds.), Forest Hydrology and Biogeochemistry: Synthesis of Past Research and Future Directions. Springer Netherlands, Dordrecht, pp. 203–219.

Andreas, W., Agata, S., Daniel, U., Karl, S., 2017. Sedimentological and ichnological implications of rapid Holocene flooding of a gently sloping mud-dominated incised valley – an example from the Red River (Gulf of Tonkin). Sedimentology 64, 1173–1202.

Baisden, W.T., Prior, C.A., Chambers, D., Canessa, S., Phillips, A., Bertrand, C., Zondervan, A., Turnbull, J.C., Kaiser, J., Bruhn, F., 2013. Rafter radiocarbon sample preparation and data flow: Accommodating enhanced throughput and precision. Nucl. Instrum. Methods Phys. Res., Sect. B 294, 194–198.

Barber, D.C., Dyke, A., Hillaire-Marcel, C., Jennings, A.E., Andrews, J.T., Kerwin, M.W., Bilodeau, G., McNeely, R., Southon, J., Morehead, M.D., Gagnon, J.M., 1999. Forcing of the cold event of 8,200 years ago by catastrophic drainage of Laurentide lakes. Nature 400, 344–348.

Berkeley, A., Perry, C.T., Smithers, S.G., Horton, B.P., Taylor, K.G., 2007. A review of the ecological and taphonomic controls on foraminiferal assemblage development in intertidal environments. Earth Sci. Rev. 83, 205–230.

Bernhardt, C.E., Horton, B.P., Stanley, J.-D., 2012. Nile Delta vegetation response to Holocene climate variability. Geology 40, 615–618.

Bidorn, B., Sok, K., Bidorn, K., Burnett, W.C., 2021. An analysis of the factors responsible for the shoreline retreat of the Chao Phraya Delta (Thailand). Sci. Total Environ. 769, 145253.

Bird, M.I., Fifield, L.K., Teh, T.S., Chang, C.H., Shirlaw, N., Lambeck, K., 2007. An inflection in the rate of early mid-Holocene eustatic sea-level rise: A new sea-level curve from Singapore. Estuarine. Coast. Shelf Sci. 71, 523–536.

Bird, M.I., Pang, W.C., Lambeck, K., 2006. The age and origin of the Straits of Singapore. Palaeogeogr. Palaeoclimatol. Palaeoecol. 241, 531–538.

Bird, M.I., Austin, W.E.N., Wurster, C.M., Fifield, L.K., Mojtahid, M., Sargeant, C., 2010. Punctuated eustatic sea-level rise in the early mid-Holocene. Geology 38, 803–806.

Bird, M.I., Brand, M., Diefendorf, A.F., Haig, J.L., Hutley, L.B., Levchenko, V., Ridd, P.V., Rowe, C., Whinney, J., Wurster, C.M., Zwart, C., 2019. Identifying the 'savanna' signature in lacustrine sediments in northern Australia. Quat. Sci. Rev. 203, 233–247.

Blott, S.J., Croft, D.J., Pye, K., Saye, S.E., Wilson, H.E., 2004. Particle size analysis by laser diffraction. Geol. Soc. Lond. Spec. Publ. 232, 63–73.

Blum, M.D., Roberts, H.H., 2009. Drowning of the Mississippi Delta due to insufficient sediment supply and global sea-level rise. Nat. Geosci. 2, 488–491.

Bouillon, S., Connolly, R.M., Lee, S.Y., 2008. Organic matter exchange and cycling in mangrove ecosystems: Recent insights from stable isotope studies. J. Sea Res. 59, 44–58.

Bova, S., Rosenthal, Y., Liu, Z., Godad, S.P., Yan, M., 2021. Seasonal origin of the thermal maxima at the Holocene and the last interglacial. Nature 589, 548–553.

Bradley, S.L., Milne, G.A., Horton, B.P., Zong, Y., 2016. Modelling Sea level data from China and Malay-Thailand to estimate Holocene ice-volume equivalent sea level change. Quat. Sci. Rev. 137, 54–68.

Cahill, N., Kemp, A.C., Horton, B.P., Parnell, A.C., 2015. Modeling Sea-level change using errors-in-variables integrated Gaussian processes. Ann. Appl. Stat. 9, 547–571.

Carvalho, R.C., Woodroffe, C.D., 2020. Evolution from estuary to delta: Alluvial plain morphology and sedimentary characteristics of the Shoalhaven River mouth, southeastern Australia. Estuar. Coast. Shelf Sci. 242, 106857.

Catalao, J., Raju, D., Nico, G., 2020. Insar Maps of Land subsidence and Sea Level scenarios to quantify the flood inundation risk in coastal cities: the case of Singapore. Remote Sens. 12, 296.

Chew, S., Wei, J., 1980. Major reclamation scheme for Marina city, Singapore. Coast. Eng. 1980, 2245–2260.

Chia, L.S., Khan, H., Chou, L.M., 1988. The Coastal Environmental Profile of Singapore. WorldFish.

Chua, S., Switzer, A.D., Kearsey, T.I., Bird, M.I., Rowe, C., Chiam, K., Horton, B.P., 2020. A new Quaternary stratigraphy of the Kallang River Basin, Singapore: Implications for urban development and geotechnical engineering in Singapore. J. Asian Earth Sci. 200, 104430.

Chua, S., Switzer, A.D., Li, T., Chen, H., Christie, M., Shaw, T.A., Khan, N.S., Bird, M.I., Horton, B.P., 2021. A new Holocene Sea-level record for Singapore. The Holocene 09596836211019096.

Corlett, R.T., 1992. The ecological transformation of Singapore, 1819-1990. J. Biogeogr. 411–420.

Cronin, T.M., Vogt, P.R., Willard, D.A., Thunell, R., Halka, J., Berke, M., Pohlman, J., 2007. Rapid sea level rise and ice sheet response to 8,200-year climate event. Geophys. Res. Lett. 34.

Di Nitto, D., Neukermans, G., Koedam, N., Defever, H., Pattyn, F., Kairo, J.G., Dahdouh-Guebas, F., 2014. Mangroves facing climate change: landward migration potential in response to projected scenarios of sea level rise. Biogeosciences 11, 857–871.

Dladla, N.N., Green, A.N., Cooper, J.A.G., Mehlhorn, P., Haberzettl, T., 2021. Bayhead delta evolution in the context of late Quaternary and Holocene Sea-level change, Richards Bay, South Africa. Mar. Geol. 441, 106608.

Dodd, T.J.H., Gillespie, M.R., Leslie, A.G., Kearsey, T.I., Kendall, R.S., Bide, T.P., Dobbs, M.R., Millar, I.L., Lee, M.K.W., Chiam, K., Goay, M., 2019. Paleozoic to Cenozoic sedimentary bedrock geology and lithostratigraphy of Singapore. J. Asian Earth Sci. 180.

Duong, N.T., Lieu, N.T.H., Cuc, N.T.T., Saito, Y., Huong, N.T.M., Phuong, N.T.M., Thuy, A.T., 2020. Holocene paleoshoreline changes of the Red River Delta, Vietnam. Rev. Palaeobot. Palynol. 278, 104235.

Fox-Kemper, B., Hewitt, H., Xiao, C., Aðalgeirsdóttir, G., Drijfhout, S., Edwards, T., Golledge, N., Hemer, M., Kopp, R., Krinner, G., 2021. Ocean, cryosphere and sea level change. In: Masson-Delmotte, V.P.Z., Pirani, A., Connors, S.L., Péan, C., Berger, S., Caud, N., Chen, Y., Goldfarb, L., Gomis, M.I., Huang, M., Leitzell, K., Lonnoy, E., Matthews, J.B.R., Maycock, T.K., Waterfield, T., Yelekçi, O., Yu, R., Zhou, B. (Eds.), Climate Change 2021: The Physical Science Basis. Contribution of Working Group I to the Sixth Assessment Report of the Intergovernmental Panel on Climate Change. Cambridge University Press.

Gao, L., Long, H., Zhang, P., Tamura, T., Feng, W., Mei, Q., 2019. The sedimentary evolution of Yangtze River delta since MIS3: a new chronology evidence revealed by OSL dating. Quat. Geochronol. 49, 153–158.

Gaw, Yee, Richards, 2019. A high-resolution map of Singapore's terrestrial ecosystems. Data 4.

Gillespie, M.R., Kendall, R.S., Leslie, A.G., Millar, I.L., Dodd, T.J.H., Kearsey, T.I., Bide, T.P., Goodenough, K.M., Dobbs, M.R., Lee, M.K.W., Chiam, K., 2019. The igneous rocks of Singapore: New insights to Palaeozoic and Mesozoic assembly of the Sukhothai Arc. J. Asian Earth Sci. 183.

Giosan, L., Naing, T., Min Tun, M., Clift, P.D., Filip, F., Constantinescu, S., Khonde, N., Blusztajn, J., Buylaert, J.-P., Stevens, T., Thwin, S., 2018. On the Holocene evolution of the Ayeyawady megadelta. Earth Surf. Dyn. 6, 451–466.

Hanebuth, T.J.J., Stattegger, K., Bojanowski, A., 2009. Termination of the last Glacial Maximum Sea-level lowstand: the Sunda-Shelf data revisited. Glob. Planet. Chang. 66, 76–84.

Guerit, L., Foreman, B.Z., Chen, C., Paola, C., Castelltort, S., 2020. Autogenic delta progradation during sea-level rise within incised valleys. Geology 49, 273–277.

Hanebuth, T.J.J., Proske, U., Saito, Y., Nguyen, V.L., Ta, T.K.O., 2012. Early growth stage of a large delta — Transformation from estuarine-platform to deltaic-progradational conditions (the northeastern Mekong River Delta, Vietnam). Sediment. Geol. 261–262, 108–119.

Haque, M.M., Hoyanagi, K., 2021. Influences of sea level on depositional environment during the last 1000 years in the southwestern Bengal delta, Bangladesh. The Holocene 31, 915–925.

Haug, G.H., Hughen, K.A., Sigman, D.M., Peterson, L.C., Röhl, U., 2001. Southward Migration of the Intertropical Convergence Zone through the Holocene. Science 293, 1304–1308.

Heaton, T.J., Köhler, P., Butzin, M., Bard, E., Reimer, R.W., Austin, W.E.N., Bronk Ramsey, C., Grootes, P.M., Hughen, K.A., Kromer, B., Reimer, P.J., Adkins, J., Burke, A., Cook, M.S., Olsen, J., Skinner, L.C., 2020. MARINE20—THE MARINE RADIOCARBON AGE CALIBRATION CURVE (0–55,000 CAL BP). Radiocarbon 1–42.

Hijma, M.P., Cohen, K.M., 2010. Timing and magnitude of the sea-level jump preluding the 8200 yr event. Geology 38, 275–278.

Hori, K., Saito, Y., 2007. An early Holocene Sea-level jump and delta initiation. Geophys. Res. Lett. 34, 5.

Hori, K., Tanabe, S., Saito, Y., Haruyama, S., Nguyen, V., Kitamura, A., 2004. Delta initiation and Holocene Sea-level change: example from the Song Hong (Red River) delta, Vietnam. Sediment. Geol. 164, 237–249.

Horton, B.P., Whittaker, J.E., Thomson, K.H., Hardbattle, M.I., Kemp, A., Woodroffe, S. A., Wright, M.R., 2005. The development of a modern foraminiferal data set for sea-level reconstructions, Wakatobi Marine National Park, Southeast Sulawesi, Indonesia. J. Foraminiferal Res. 35, 1–14.

Hu, D., Clift, P.D., Böning, P., Hannigan, R., Hillier, S., Blusztajn, J., Wan, S., Fuller, D.Q., 2013. Holocene evolution in weathering and erosion patterns in the Pearl River delta. Geochem. Geophys. Geosystems. 14, 2349–2368.

Ishii, Y., Tamura, T., Ben, B., 2021. Holocene sedimentary evolution of the Mekong River floodplain, Cambodia. Quat. Sci. Rev. 253.

Kern, O.A., Koutsodendris, A., Machtle, B., Christanis, K., Schukraft, G., Scholz, C., Kotthoff, U., Pross, J., 2019. XRF core scanning yields reliable semiquantitative data on the elemental composition of highly organic-rich sediments: evidence from the Furamoos peat bog (Southern Germany). Sci. Total Environ. 697, 134110.

Khan, N.S., Vane, C.H., Horton, B.P., Hillier, C., Riding, J.B., Kendrick, C.P., 2015b. The application of δ13C, TOC and C/N geochemistry to reconstruct Holocene relative sea levels and paleoenvironments in the Thames Estuary, UK. J. Quat. Sci. 30, 417–433.

Kuehl, S.A., Nittrouer, C.A., DeMaster, D.J., 1986. Distribution of sedimentary structures in the Amazon subaqueous delta. Cont. Shelf Res. 6, 311–336.

Lamb, A.L., Vane, C.H., Wilson, G.P., Rees, J.G., Moss-Hayes, V.L., 2007. Assessing δ13C and C/N ratios from organic material in archived cores as Holocene Sea level and palaeoenvironmental indicators in the Humber Estuary, UK. Mar. Geol. 244, 109–128.

Lambeck, K., Rouby, H., Purcell, A., Sun, Y., Sambridge, M., 2014. Sea level and global ice volumes from the Last Glacial Maximum to the Holocene. Proc. Natl. Acad. Sci. 111, 15296–15303.
Lap Nguyen, V., Ta, T.K.O., Tateishi, M., 2000. Late Holocene depositional environments and coastal evolution of the Mekong River Delta, Southern Vietnam. J. Asian Earth Sci. 18, 427–439.
Leonardi, N., Mei, X., Carnacina, I., Dai, Z., 2021. Marine sediment sustains the accretion of a mixed fluvial-tidal delta. Mar. Geol. 438, 106520.
Leslie, A.G., Dobbs, M.R., Dodd, T.J., Gillespie, M.R., Kearsey, T.I., Kendall, R.S., Lewis, M.A., Bide, T.P., Millar, I.L., Chua, S., Switzer, A.D., Chiam, S.L., Goay, K.H., Lau, S.G., Lim, Y.S., Zaw, M.H., Kyaw, K.Z., 2021. Singapore Geology (2021): Memoir of the Bedrock, Superficial and Engineering Geology., Singapore.
Leslie, A.G., Dodd, T.J.H., Gillespie, M.R., Kendall, R.S., Bide, T.P., Kearsey, T.I., Dobbs, M.R., Lee, M.K.W., Chiam, K., 2019. Ductile and brittle deformation in Singapore: A record of Mesozoic orogeny and amalgamation in Sundaland, and of post-orogenic faulting. J. Asian Earth Sci. 181, 1–18.
Lovelock, C.E., Adame, M.F., Bennion, V., Hayes, M., Reef, R., Santini, N., Cahoon, D.R., 2015. Sea level and turbidity controls on mangrove soil surface elevation change. Estuarine. Coast. Shelf Sci. 153, 1–9.
Luan, H.L., Ding, P.X., Yang, S.L., Wang, Z.B., 2021. Accretion-erosion conversion in the subaqueous Yangtze Delta in response to fluvial sediment decline. Geomorphology 382.
Marcott, S.A., Shakun, J.D., Clark, P.U., Mix, A.C., 2013. A reconstruction of regional and global temperature for the past 11,300 years. Science 339, 1198–1201.
McSweeney, S., Stout, J., Savige, T., 2021. Basin infill increases seaward sediment delivery in small, tide-dominated estuaries. Estuar. Coast. Shelf Sci. 258, 107441.
Minhat, F.I., Satyanarayana, B., Husain, M.-L., Rajan, V.V., 2016. Modern benthic Foraminifera in subtidal waters of Johor: Implications for Holocene Sea-level change on the east coast of peninsular Malaysia. J. Foraminiferal Res. 46, 347–357.
Morrill, C., Jacobsen, R.M., 2005. How widespread were climate anomalies 8200 years ago? Geophys. Res. Lett. 32.
Muto, T., Steel, R.J., 1997. Principles of regression and transgression; the nature of the interplay between accommodation and sediment supply. J. Sediment. Res. 67, 994–1000.
Nguyen, V.L., Ta, T.K.O., Saito, Y., 2010. Early Holocene initiation of the Mekong River delta, Vietnam, and the response to Holocene Sea-level changes detected from DT1 core analyses. Sediment. Geol. 230, 146–155.
Nicholls, R.J., Lincke, D., Hinkel, J., Brown, S., Vafeidis, A.T., Meyssignac, B., Hanson, S. E., Merkens, J.-L., Fang, J., 2021. A global analysis of subsidence, relative sea-level change and coastal flood exposure. Nat. Clim. Chang. 11, 338–342.
Nienhuis, J.H., van de Wal, R.S.W., 2021. Projections of global delta land loss from sea-level rise in the 21st century. Geophys. Res. Lett. 48, e2021GL093368.
Parnell, A., Parnell, M.A., 2020. Package 'Bchron'.
Pennington, B.T., Sturt, F., Wilson, P., Rowland, J., Brown, A.G., 2017. The fluvial evolution of the Holocene Nile Delta. Quat. Sci. Rev. 170, 212–231.
Pérez, A., Gutiérrez, D., Saldarriaga, M.S., Sanders, C.J., 2017. Hydrological controls on the biogeochemical dynamics in a Peruvian mangrove forest. Hydrobiologia 803, 69–86.
Powell, M.A., 2020. Singapore's lost Coast: Land Reclamation, National Development and the Erasure of Human and Ecological Communities, 1822–Present. In: Environment and History.
Reimer, P.J., Austin, W.E.N., Bard, E., Bayliss, A., Blackwell, P.G., Bronk Ramsey, C., Butzin, M., Cheng, H., Edwards, R.L., Friedrich, M., Grootes, P.M., Guilderson, T.P., Hajdas, I., Heaton, T.J., Hogg, A.G., Hughen, K.A., Kromer, B., Manning, S.W., Muscheler, R., Palmer, J.G., Pearson, C., van der Plicht, J., Reimer, R.W., Richards, D.A., Scott, E.M., Southon, J.R., Turney, C.S.M., Wacker, L., Adolphi, F., Büntgen, U., Capano, M., Fahrni, S.M., Fogtmann-Schulz, A., Friedrich, R., Köhler, P., Kudsk, S., Miyake, F., Olsen, J., Reinig, F., Sakamoto, M., Sookdeo, A., Talamo, S., 2020. THE INTCAL20 NORTHERN HEMISPHERE RADIOCARBON AGE CALIBRATION CURVE (0–55 CAL kBP). Radiocarbon 1–33.
Reimer, R.W., Reimer, P.J., 2017. An online application for ΔR calculation. Radiocarbon 59, 1623–1627.
Revel, M., Ducassou, E., Skonieczny, C., Colin, C., Bastian, L., Bosch, D., Migeon, S., Mascle, J., 2015. 20,000 years of Nile River dynamics and environmental changes in the Nile catchment area as inferred from Nile upper continental slope sediments. Quat. Sci. Rev. 130, 200–221.
Richter, T.O., Van Der Gaast, S., Koster, B., Vaars, A., Gieles, R., De Stigter, H.C., De Haas, H., Van Weering, T.C.E., 2006. In: Rothwell, R.G. (Ed.), The Avaatech XRF Core Scanner: Technical description and applications to NE Atlantic sediments. Geological Society Special Publication, pp. 39–50.
Rodriguez, A.B., Simms, A.R., Anderson, J.B., 2010. Bay-head deltas across the northern Gulf of Mexico back step in response to the 8.2ka cooling event. Quat. Sci. Rev. 29, 3983–3993.
Rogers, K., 2021. Accommodation space as a framework for assessing the response of mangroves to relative sea-level rise. Singap. J. Trop. 42, 163–183.
Rothwell, R.G., Croudace, I.W., 2015. Twenty Years of XRF Core Scanning Marine Sediments: What Do Geochemical Proxies Tell Us?, 17, pp. 25–102.
Ryżak, M., Bieganowski, A., 2011. Methodological aspects of determining soil particle-size distribution using the laser diffraction method. J. Plant Nutr. Soil Sci. 174, 624–633.
Saintilan, N., Khan, N.S., Ashe, E., Kelleway, J.J., Rogers, K., Woodroffe, C.D., Horton, B. P., 2020. Thresholds of mangrove survival under rapid sea level rise. Science 368, 1118–1121.
Sarr, A.-C., Husson, L., Sepulchre, P., Pastier, A.-M., Pedoja, K., Elliot, M., Arias-Ruiz, C., Solihuddin, T., Aribowo, S., 2019. Subsiding sundaland. Geology 47, 119–122.
Schimanski, A., Stattegger, K., 2005. Deglacial and Holocene evolution of the Vietnam shelf: stratigraphy, sediments and sea-level change. Mar. Geol. 214, 365–387.
Shaw, T.A., Li, T., Ng, T., Cahill, N., Chua, S., Majewski, J.M., Nathan, Y., Garner, G.G., Kopp, R.E., Hanebuth, T.J., 2023. Deglacial perspectives of future sea level for Singapore. Commun. Earth Environ. 4, 204.
Simms, A.R., Rodriguez, A.B., 2014. Where do coastlines stabilize following rapid retreat? Geophys. Res. Lett. 41, 1698–1703.
Simons, W.J.F., Socquet, A., Vigny, C., Ambrosius, B.A.C., Haji Abu, S., Promthong, C., Subarya, C., Sarsito, D.A., Matheussen, S., Morgan, P., Spakman, W., 2007. A decade of GPS in Southeast Asia: Resolving Sundaland motion and boundaries. J. Geophys. Res. Solid Earth 112.
Sinsakul, S., 2000. Late Quaternary geology of the lower Central Plain, Thailand. J. Asian Earth Sci. 18, 415–426.
Song, B., Li, Z., Saito, Y., Okuno, J.i., Li, Z., Lu, A., Hua, D., Li, J., Li, Y., Nakashima, R., 2013. Initiation of the Changjiang (Yangtze) delta and its response to the mid-Holocene Sea level change. Palaeogeogr. Palaeoclimatol. Palaeoecol. 388, 81–97.
Stanley, D.J., Warne, A.G., 1994. Worldwide Initiation of Holocene Marine Deltas by Deceleration of Sea-Level rise. Science 265, 228–231.
Storms, J.E.A., Hoogendoorn, R.M., Dam, R.A.C., Hoitink, A.J.F., Kroonenberg, S.B., 2005. Late-Holocene evolution of the Mahakam delta, East Kalimantan, Indonesia. Sediment. Geol. 180, 149–166.
Stroeven, A.P., Hättestrand, C., Kleman, J., Heyman, J., Fabel, D., Fredin, O., Goodfellow, B.W., Harbor, J.M., Jansen, J.D., Olsen, L., Caffee, M.W., Fink, D., Lundqvist, J., Rosqvist, G.C., Strömberg, B., Jansson, K.N., 2016. Deglaciation of Fennoscandia. Quat. Sci. Rev. 147, 91–121.
Suriadi, R., Shaari, H., Culver, S.J., Husain, M.L., Vijayan, V., Parham, P.R., Sulaiman, A., Sapon, N., 2019. Inner shelf benthic foraminifera of the South China Sea, east coast Peninsular Malaysia. J. Foraminifer. Res. 49, 11–28.
Switzer, A.D., Pile, J., 2015. Grain Size Analysis, Handbook of Sea-Level Research. John Wiley & Sons, Ltd, pp. 331–346.
Syvitski, J.P.M., Kettner, A.J., Overeem, I., Hutton, E.W.H., Hannon, M.T., Brakenridge, G.R., Day, J., Vörösmarty, C., Saito, Y., Giosan, L., Nicholls, R.J., 2009. Sinking deltas due to human activities. Nat. Geosci. 2, 681–686.
Ta, T.K.O., Nguyen, V.L., Tateishi, M., Kobayashi, I., Tanabe, S., Saito, Y., 2002. Holocene delta evolution and sediment discharge of the Mekong River, southern Vietnam. Quat. Sci. Rev. 21, 1807–1819.
Tamura, T., Saito, Y., Sieng, S., Ben, B., Kong, M., Sim, I., Choup, S., Akiba, F., 2009. Initiation of the Mekong River delta at 8 ka: evidence from the sedimentary succession in the Cambodian lowland. Quat. Sci. Rev. 28, 327–344.
Tanabe, S., 2003. Song Hong (Red River) delta evolution related to millennium-scale Holocene Sea-level changes. Quat. Sci. Rev. 22, 2345–2361.
Tanabe, S., Saito, Y., Sato, Y., Suzuki, Y., Sinsakul, S., Tiyapairach, S., Chaimanee, N., 2003. Stratigraphy and Holocene evolution of the mud-dominated Chao Phraya delta, Thailand. Quat. Sci. Rev. 22, 789–807.
Tanabe, S., Saito, Y., Lan Vu, Q., Hanebuth, T.J.J., Lan Ngo, Q., Kitamura, A., 2006. Holocene evolution of the Song Hong (Red River) delta system, northern Vietnam. Sediment. Geol. 187, 29–61.
Tessler, Z.D., Vörösmarty, C.J., Overeem, I., Syvitski, J.P.M., 2018. A model of water and sediment balance as determinants of relative sea level rise in contemporary and future deltas. Geomorphology 305, 209–220.
Thanh, N.T., Cuong, D.H., Stattegger, K., Dung, B.V., Yang, S., Chi, N.T.K., Tung, N.X., Tinh, N.V., Nga, N.T., 2021. Depositional sequences of the Mekong river delta and adjacent shelf over the past 140 kyr, southern Vietnam. J. Asian Earth Sci. 206.
Thiry, M., 2000. Palaeoclimatic interpretation of clay minerals in marine deposits: an outlook from the continental origin. Earth Sci. Rev. 49, 201–221.
Thomas, E.R., Wolff, E.W., Mulvaney, R., Steffensen, J.P., Johnsen, S.J., Arrowsmith, C., White, J.W.C., Vaughn, B., Popp, T., 2007. The 8.2ka event from Greenland ice cores. Quat. Sci. Rev. 26, 70–81.
Tjallingii, R., Röhl, U., Kölling, M., Bickert, T., 2007. Influence of the water content on X-ray fluorescence core-scanning measurements in soft marine sediments. Geochem. Geophys. Geosyst. 8 n/a-n/a.
Tjallingii, R., Stattegger, K., Wetzel, A., Van Phach, P., 2010. Infilling and flooding of the Mekong River incised valley during deglacial sea-level rise. Quat. Sci. Rev. 29, 1432–1444.
Tjia, H.D., Liew, K.K., 1996. Changes in tectonic stress field in northern Sunda Shelf basins. Geol. Soc. Lond. Spec. Publ. 106, 291–306.
Törnqvist, T.E., Bick, S.J., González, J.L., van der Borg, K., de Jong, A.F.M., 2004. Tracking the sea-level signature of the 8.2 ka cooling event: New constraints from the Mississippi Delta. Geophys. Res. Lett. 31.
Törnqvist, T.E., Jankowski, K.L., Li, Y.-X., González, J.L., 2020. Tipping points of Mississippi Delta marshes due to accelerated sea-level rise. Sci. Adv. 6, eaaz5512.
Törnqvist, T.E., Cahoon, D.R., Morris, J.T., Day, J.W., 2021. Coastal wetland resilience, accelerated sea-level rise, and the importance of timescale. AGU Adv. 2, e2020AV000334.
Tue, N.T., Thai, N.D., Nhuan, M.T., 2020. Carbon storage potential of mangrove forests from Northeastern Vietnam. Reg. Stud. Mar. Sci. 40, 101516.
Ullman, D.J., Carlson, A.E., Hostetler, S.W., Clark, P.U., Cuzzone, J., Milne, G.A., Winsor, K., Caffee, M., 2016. Final Laurentide ice-sheet deglaciation and Holocene climate-sea level change. Quat. Sci. Rev. 152, 49–59.
Wang, Z., Saito, Y., Zhan, Q., Nian, X., Pan, D., Wang, L., Chen, T., Xie, J., Li, X., Jiang, X., 2018. Three-dimensional evolution of the Yangtze River mouth, China during the Holocene: impacts of sea level, climate and human activity. Earth Sci. Rev. 185, 938–955.
Wang, Z., Zhuang, C., Saito, Y., Chen, J., Zhan, Q., Wang, X., 2012. Early mid-Holocene sea-level change and coastal environmental response on the southern Yangtze delta plain, China: implications for the rise of Neolithic culture. Quat. Sci. Rev. 35, 51–62.

Wilson, G.P., 2017. On the application of contemporary bulk sediment organic carbon isotope and geochemical datasets for Holocene sea-level reconstruction in NW Europe. Geochim. Cosmochim. Acta. 214, 191–208.
Wilson, G.P., Lamb, A.L., Leng, M.J., Gonzalez, S., Huddart, D., 2005. δ13C and C/N as potential coastal palaeoenvironmental indicators in the Mersey Estuary, UK. Quat. Sci. Rev. 24, 2015–2029.
Winterwerp, J.C., 2002. On the flocculation and settling velocity of estuarine mud. Cont. Shelf Res. 22, 1339–1360.
Wong, P.P., 1992. Impact of a sea level rise on the coasts of Singapore: preliminary observations. J. SE Asian Earth Sci. 7, 65–70.
Woodroffe, C.D., Rogers, K., McKee, K.L., Lovelock, C.E., Mendelssohn, I.A., Saintilan, N., 2016. Mangrove Sedimentation and Response to Relative Sea-Level Rise. Ann. Rev. Mar. Sci. 8, 243–266.
Wurtzel, J.B., Abram, N.J., Lewis, S.C., Bajo, P., Hellstrom, J.C., Troitzsch, U., Heslop, D., 2018. Tropical Indo-Pacific hydroclimate response to North Atlantic forcing during the last deglaciation as recorded by a speleothem from Sumatra, Indonesia. Earth Planet. Sci. Lett. 492, 264–278.
Xue, Z., Liu, J.P., DeMaster, D., Van Nguyen, L., Ta, T.K.O., 2010. Late Holocene Evolution of the Mekong Subaqueous Delta, Southern Vietnam. Mar. Geol. 269, 46–60.
Yen, H.P.H., Nhan, T.T.T., Nghi, T., Toan, N.Q., Khien, H.A., Lam, D.D., Van Long, H., Thanh, D.X., Hung, N.T., Trang, N.T.H., Dien, T.N., Tuyen, N.T., Truong, T.X., Dung, T.T., Thao, N.T.P., Lan, V.Q., 2021. Late Pleistocene-Holocene sedimentary evolution in the coastal zone of the Red River Delta. Heliyon 7, e05872.
Yu, F., Zong, Y., Lloyd, J.M., Huang, G., Leng, M.J., Kendrick, C., Lamb, A.L., Yim, W.W. S., 2010. Bulk organic δ13C and C/N as indicators for sediment sources in the Pearl River delta and estuary, southern China. Estuar. Coast. Shelf Sci. 87, 618–630.
Yu, F., Zong, Y., Lloyd, J.M., Leng, M.J., Switzer, A.D., Yim, W.W.S., Huang, G., 2011. Mid-Holocene variability of the East Asian monsoon based on bulk organic δ13C and C/N records from the Pearl River estuary, southern China. The Holocene 22, 705–715.
Zhan, Q., Li, M., Liu, X., Chen, J., Chen, Z., 2020. Sedimentary transition of the Yangtze subaqueous delta during the past century: Inspiration for delta response to future decline of sediment supply. Mar. Geol. 428, 106279.
Zong, Y., Huang, K., Yu, F., Zheng, Z., Switzer, A., Huang, G., Wang, N., Tang, M., 2012. The role of sea-level rise, monsoonal discharge and the palaeo-landscape in the early Holocene evolution of the Pearl River delta, southern China. Quat. Sci. Rev. 54, 77–88.